THESIS FOR THE DEGREE OF DOCTOR OF PHILOSOPHY

Large-Eddy Simulations for Computing the Flow Around Vehicles

SINIŠA KRAJNOVIĆ

Department of Thermo and Fluid Dynamics
CHALMERS UNIVERSITY OF TECHNOLOGY
Göteborg, Sweden, 2002

Large-Eddy Simulations for Computing the Flow Around Vehicles
SINIŠA KRAJNOVIĆ
ISBN 91-7291-188-3

© SINIŠA KRAJNOVIĆ, 2002

Doktorsavhandlingar vid Chalmers tekniska högskola
Ny serie nr 1870
ISSN 0346-718X

Institutionen för termo- och fluiddynamik
Chalmers tekniska högskola
SE-412 96 Göteborg, Sweden
Phone +46-(0)31-7721400
Fax: +46-(0)31-180976

Cover:
Flow around a simplified bus. Time-averaged flow is shown on the right and the instantaneous flow on the left of the center plane of the bus. Instantaneous coherent structures are visualized using the isosurfaces of the second invariant of the velocity gradient and pressure. Time-averaged trace lines coloured with static pressure are used to visualize the time-averaged flow patterns.

Printed at Chalmers Reproservice
Göteborg, Sweden 2002

Large-Eddy Simulations for Computing the Flow Around Vehicles

by

SINIŠA KRAJNOVIĆ

Department of Thermo and Fluid Dynamics
Chalmers University of Technology
SE-412 96 Göteborg, Sweden

Abstract

The feasibility of the use of large-eddy simulation (LES) in external vehicle aerodynamics is investigated. The computational requirement for LES of the full size car at road conditions is beyond the capability of computers in the near future. Since LES cannot be used for quantitative prediction of this flow, i.e. obtaining the aerodynamic forces and moments, an alternative use of LES is suggested than can be useful in increasing our understanding of the flow around a car. It is found that making LES of the flow around simplified car-like shapes at lower Reynolds numbers can increase our knowledge of the flow around a car. Two simulations are made, one of the flow around a cube and the other of the flow around a simplified bus. The former simulation proved that LES with a relatively coarse resolution and simple inlet boundary condition can provide accurate results. The latter simulation resulted in a flow that agrees with experimental observations and displayed some flow features that were not observed in the experiments or steady simulations of such flows. This simulation afforded us the possibility to study the transient mechanisms that are responsible for the aerodynamic properties of a car. The knowledge gained from this simulation can be used by the stylist to tune the aerodynamics of the car's design as well as by CFD specialists to improve turbulence models.

A mixed one-equation subgrid-scale model for LES is proposed. A new model is constructed following the observation that the chief transport of turbulent energy is a local process that occurs between the scales closest to the cut-off. This transport of energy is modeled with the scale-similarity part and the remaining non-local energy transport is represented with the eddy viscosity part.

List of Publications

I am the first author of all papers and all work presented in the papers has been carried out by myself. I have analyzed and discussed the contents of the papers with my supervisor, Professor Lars Davidson. The contribution of Dirk Müller to Paper I was LES of the flow in a ventilated room; these results were later removed from the paper at the request of the reviewers in order to reduce the length of the paper.

This thesis is based on the work contained in the following papers:

I. S. Krajnović and L. Davidson
"Comparison of two one-equation subgrid models in recirculating flows"
In Proceedings of *Direct and Large-Eddy Simulation III*, Eds: P.V. Voke, N.D. Sandham and L. Kleiser, pages 63-74, 1999.

II. S. Krajnović and L. Davidson
"Large-eddy simulation of the flow around a surface-mounted cube using a dynamic one-equation subgrid model"
In Proceedings of *The First International Symposium on Turbulence and Shear Flow Phenomena*, Santa Barbara, Eds: S. Banerjee & J.K. Eaton, begell house, inc., New York, Wallingford U.K., pages 741-746, 1999.

III. S. Krajnović and L. Davidson
"Flow around a three-dimensional bluff body"
In Proceedings of the *9th International Symposium on Flow Visualisation*, Heriot-Watt University, Edinburgh, G.M. Carlomagno and I. Grant (Eds.), 2000.

IV. S. Krajnović and L. Davidson
"Large-Eddy Simulation of the Flow Around a Three-Dimensional Bluff Body"
AIAA paper 2001–0432, Reno, NV, 2001.

V. S. Krajnović and L. Davidson
"Large-Eddy Simulation of the Flow Around a Ground Vehicle Body"
SAE Paper 2001-01-0702, Detroit, 2001.

VI. S. Krajnović and L. Davidson
"Large-Eddy Simulations of the Flow Around A Simplified Bus"
In Proceedings of the *3rd AFOSR International Conference on DNS and LES*, Eds: C. Liu and L. Sakell and T. Beutner, Arlington, Texas, pages 775-782, 2001.

VII. S. Krajnović and L. Davidson
"Large-Eddy Simulation of the Flow Around a Bluff Body"
AIAA Journal, 40(5), pages 927-139, 2002.

VIII. S. Krajnović and L. Davidson
"A mixed one-equation subgrid model for large-eddy simulation"
International Journal of Heat and Fluid Flow, 23(4), pages 413–245, 2002.

IX. S. Krajnović and L. Davidson
"A test case for large-eddy simulation in vehicle aerodynamics"
In Proceedings of the *5th International Symposium on Engineering Turbulence Modelling and Measurements*, Mallorca, Spain, 2002.

X. S. Krajnović and L. Davidson
"Numerical study of the flow around the bus-shaped body"
Submitted for journal publication.

Acknowledgments

I would like to express my sincere gratitude to my supervisor, Professor Lars Davidson, for his scientific and technical guidance and his support during my graduate studies.

Recognition is due to Dr. Mats Ramnefors for initiating this project together with my supervisor and showing interest in my research during his time at Volvo Car Corporation.

I would like to acknowledge Sven Perzon for doing most of the administrative work for the financing of my project. We have also had lengthy technical discussions, and he made my visits at Volvo Car Corporation very enjoyable.

I would also like to thank Dr. Magnus Olsson for supporting this project and making valuable comments.

The support of the National Swedish Board for Technical Development (NUTEK), the Swedish Agency for Innovation Systems (VINNOVA) and Volvo Car Corporation is gratefully acknowledged.

I would like to express thanks to my colleges Dr. Håkan Nilsson for introducing me to ICEM CFD and Dr. Gunnar Johansson for discussions on experiments and turbulence.

Monika Davidović, thank you for all your support and love.

Contents

Chapter 1

Introduction

Although the Reynolds-averaged Navier-Stokes (RANS) equations used in the industrial prediction of the flow around cars have been relatively successful, they are far from being a design tool for external aerodynamics. Flow around a car is three-dimensional with steep pressure gradients and regions of separated flows. The numbers of vortices are not formed only along the body and in the separation bubble in the near wake but also far from the rear face of the car. Bearman [7] and Krajnović and Davidson [36] recently found large differences between time-averaged flow containing only a small number of three-dimensional vortices and the instantaneous flow containing a large number of three-dimensional vortices at different positions and of different sizes. The wide spectrum of scales in the wake region prevents the construction of an accurate RANS model. All these properties together with the high levels of unsteadiness in this flow are major obstacles to accurate prediction using RANS. One illustrative example of RANS's accuracy in vehicle aerodynamics is [24], where the flow around Ahmed's body [2] is predicted. The computed pressure at the rear vertical face of the body was (for a base slant angle smaller than 20^o) under-predicted, resulting in the computed drag being 30% higher than the measured drag [24, 27]. More accurate three-dimensional time-dependent simulation is thus needed.

Some early attempts to use transient simulations for this kind of flow are presented in [32], [26] and [3]. Although the authors of these papers denoted their simulations direct numerical simulations (DNS) [32, 26] or large-eddy simulation (LES) [3], I would classify the simulation in [3] as an unresolved LES and the simulations in [32] and [26] as uncontrolled LES. The simulation in [3] is the only simulation of this flow to my knowledge where the subgrid-scale model is employed

explicitly. Transport of energy from the resolved scales to the SGS is achieved in [32] and [26] by using a third-order upwind scheme for the convection terms. The absence of an SGS model in these simulations makes it difficult to separate resolved from modeled turbulent energy.

This paper attempts to (I) explore the suitability of LES in external vehicle aerodynamics, and (II) present an improved picture of the flow around cars based on my large-eddy simulations. In (I), I shall investigate the influence of different boundary conditions, SGS models and Reynolds number dependence on the results and suggest one way of conducting LES in near future. The purpose of (II) is to explore the flow around one car-like body and to establish two pictures of this flow: one of the instantaneous and the other of the time-averaged flow.

While the picture of the time-averaged flow may seem an obvious tool for the description of the aerodynamic properties of the car (the time-averaged description of this flow was until recently [7, 36] the only description), the prediction of the transient effects of the flow on the car can only be done using an instantaneous representation of this flow. Some examples of the transient influences of the flow are the variations of the forces and moments acting on a car that are responsible for the car's stability and thus for traffic safety and comfort, the wind generated noise and the accumulation of water and dirt on the car surface.

Chapter 2

Making LES of the flow around a car

This section discusses the feasibility of LES in vehicle aerodynamics. Some open questions in LES for this flow are presented and my personal answers on these questions are given. These questions can be summarized in the following groups: the spatial resolution, the boundary conditions and the SGS modeling.

2.1 Spatial resolution

Before we give an estimate for the computational grid, it is appropriate to present flow features that must be resolved for an accurate prediction of the flow. Flow around a car is wall-bounded, meaning that the coherent motions in the boundary layer are responsible for the maintenance of turbulence. This statement leads to two questions: what is the size of these structures and how great is their influence on the large-scale structures?

Experimental and DNS results indicate that the sublayer and buffer region of the boundary layer consist of elongated regions of high-speed and low-speed stream-wise velocity (streaks) (see Fig. 2.1). Analyses of DNS and experimental data indicate that the stream-wise size of these vortices is approximately 400 wall units according to DNS [45] and larger than 1000 wall units according to experiments [61] and that the span-wise spacing between them is approximately 100 [53] wall units. According to Robinson [53]: *"The thin, near-wall buffer region is the most important zone of the boundary layer in terms of turbulence energy production and dissipation. Buffer-region activity is characterized by a*

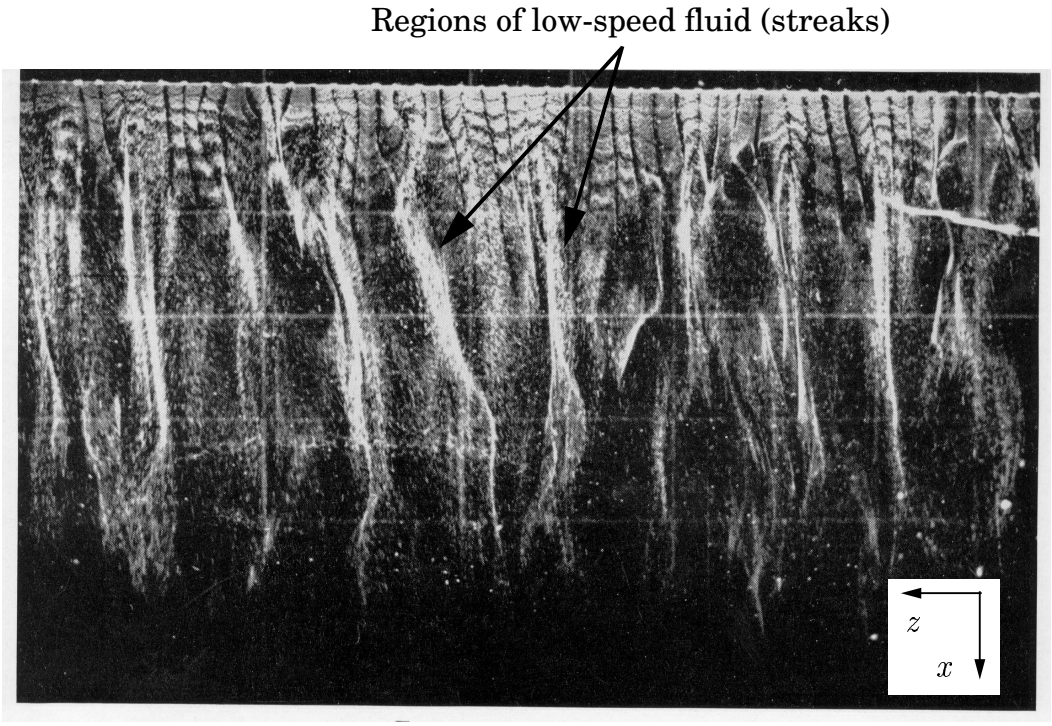

Figure 2.1: Structures in the flat plate turbulent boundary layer at $y^+ = 4.5$ (buffer layer) visualized with the hydrogen bubble technique (from [33] reproduced by permission of Cambridge University Press). x and z are the stream-wise and the span-wise directions, respectively.

bursting process, during which low-speed fluid (provided in the form of streaks) is flung outward from the wall, generating most of the turbulence production in the boundary layer." Thus accurate representation of these vortices is of importance for a prediction of the flow. Let us now consider the resolution requirements of these structures in LES. Pope [51] suggests that a grid that can resolve 80% of the turbulent energy everywhere in the domain including the viscous wall region is needed for LES with wall resolution. According to Piomelli and Chasnov [49], the first grid point must be located at $y^+ < 1$ expressed in wall units $y^+ = u_\tau y/\nu$. The resolution in the stream-wise and the span-wise directions must be $\Delta x^+ \simeq 50 - 150$, $\Delta z^+ \simeq 15 - 40$ in order to accurately represent the coherent structures in the near-wall region.

To illustrate the size of the computational grid that would be needed for the resolution suggested in [49], I constructed a computational grid for the vehicle-like body in [36]. The resolution on the body expressed

in the wall units was $\langle \Delta s^+ \rangle_t = 30 - 145$, $\langle \Delta n^+ \rangle_t = 0.5 - 0.8$ and $\langle \Delta l^+ \rangle_t = 14 - 35$. Here $\Delta f^+ = \Delta f u_\tau / \nu$, u_τ is the friction velocity and $\langle . \rangle_t$ denotes time averaging, s is the stream-wise direction, n is the wall-normal direction and l is the span-wise direction. The resulting structured grid contains 9.8×10^6 cells, of which approximately 2×10^6 cells are located in the near-wall region ($y^+ < 20$). Note that the resolution of the boundary layers on the lateral walls and the ceiling of the wind tunnel was not considered here.

Now let us extrapolate this grid to the Reynolds number of the flow around a passenger car of approximately 5×10^6 (i.e. 24 times the Reynolds number in [36]). For this purpose we estimate the dependence of the number of the nodes with the Reynolds number. Consider a small element ΔA of surface area L_x by L_z and let n_y be the number of y-direction grid points in the viscous sublayer. The number of the grid points in the near-wall region above ΔA is then

$$\Delta N = \frac{L_x L_z n_y}{\Delta x \Delta z} = \frac{n_y}{\Delta x^+ \Delta z^+} Re_\tau^2 \tag{2.1}$$

Now we introduce the skin friction coefficient,

$$C_f = \frac{2\tau_w}{\rho U_\infty^2} = 2 \left(\frac{u_\tau}{U_\infty} \right)^2 \tag{2.2}$$

Simple flat plate equation from [57] $C_f = 0.0592 Re^{-1/5}$ together with Eq. 2.2 gives

$$Re_\tau = 0.0296^{1/2} Re^{0.9} \tag{2.3}$$

The substitution of Eq. 2.3 into Eq. 2.1 gives

$$\Delta N = 0.0296 \frac{n_y}{\Delta x^+ \Delta z^+} Re^{1.8} \tag{2.4}$$

Thus the resolution requirements for the representation of the near-wall region ($y^+ < 20$) increases as $\mathcal{O}\left(Re^{1.8}\right)$ and, when the Re number is increased by a factor of 24, the number of cells in the inner region will increase by 305 times. The resulting resolution for only the near-wall region is thus approximately 0.61×10^9 cells. We should note that this is the lowest limit because the real car has a far more complex geometry than the simplified vehicle body considered in this paper and much more cells would be required for its representation. The analysis above considered only the Re number influence on the resolution in the stream-wise and span-wise directions. The number of cells in

the y-direction is also increased with the Re number, making the grid required for the flow in the near-wall region of a car very large. If we now add the number of cells in the rest of the domain, it is clear that the transient simulation of this problem is far from what can be computed with the largest existing computer (largest LES/DNS simulation done to date had $20 - 30 \times 10^6$ cells [20]).

The resolution requirements given above must be met in channel or a flat plate boundary simulations. However, in the case of a bluff-body flow, such as flow around a car, with massive separations and regions of recirculating flow, the influence of the near-wall structures on the main flow is smaller. As follows from this observation we can relax the requirement on resolution given above; even so however, the computational grid for the full-scale car flow is very large.

The following section considers the Reynolds number dependence on the flow around a car, and it will be shown that LES can be used to predict the flow around a car, although the problem must be slightly redefined.

2.2 Reynolds number dependence

As one illustration, I consider the flow around a cube mounted on a wind tunnel wall [56, 59, 34]. This flow will be discussed in more detail later in the paper. Here I will study only some results presented by Rodi *et al.* [56]. These authors presented results from the simulations of this flow at two different Reynolds numbers, 3000 and 40000, based on the incoming velocity and cube height. They found a great similarity in the results for these two flows. Time-averaged coherent structures had almost identical shapes and sizes in the two flows. Thus it seems likely that the qualitative knowledge about the flow around a three-dimensional bluff bodies (such as a car) can be extracted from the flow at lower Reynolds number. This observation is not new and has long been used for experimental studies [9, 2, 5, 18]. Note however that the choice of the lower Reynolds number, which is high enough to produce a flow similar to that around a full-scale vehicle, is not trivial.

2.3 Boundary conditions

The resolution requirements in the boundary layer presented above prevent the use of a no-slip boundary condition on the solid walls of

a real car. This does not mean that the same is valid for our redefined problem of a simplified car at lower Reynolds number. As will be shown later in the paper, this is possible and has been done for the flow around a simplified bus [37, 36]. To reduce the computational cost required when a no-slip condition is used, several models for the dynamics of the near-wall structures were suggested. Some of these models are proposed in [16], [58], [50], [4] and [10], but none has proven to be successful for complex flows with separations and regions of recirculating flow, such as the flow around a car.

In some spatially evolving (developing) flows such as the flow over the backward-facing step [21] or a diffuser flow [31], the choice of the inlet boundary condition was found to be critical for successful simulation. Two different generation techniques for inlet boundary conditions dominate. The instantaneous velocity profile at the inlet can be obtained by superimposing random noise on the mean statistical profile. However, this technique produces unphysical fluctuating velocity (for example $\langle u'v' \rangle = 0$). One way of constructing the inlet boundary condition with consistent fluctuations (i.e. similar to that in the experiment) is to make LES of a fully developed channel flow with a periodic boundary condition in the stream-wise direction, store the instantaneous velocities in one cross-sectional plane for a large number of time steps and then use these data as inflow conditions for the new simulation. It is shown [21, 31] that this technique produces very good results but its use in vehicle aerodynamics is not practical owing to the very high computational cost for their generation. Later in the paper it will be shown that, in LES of the flow around bluff bodies (such as a car), the use of much simpler stationary inflow conditions can result in accurate results.

2.4 SGS modeling

A large number of models for the SGS stress tensor have been proposed in the past four decades (see [43] for a review), most of them built on the algebraic eddy viscosity model originally proposed by Smagorinsky [60]. Here, we shall consider only the most common Smagorinsky model and its dynamic variants.

Besides the need of adjusting the Smagorinsky constant for different flows, the Smagorinsky model produces, incorrectly, non-zero SGS viscosity and shear stress at the wall. This model gives a poor prediction of the SGS stress tensor and the correlation between the SGS

stress computed from DNS and those modeled using the Smagorinsky model ranges from 0 to 0.25 [40]. The introduction of the dynamic procedure by Germano [22] improved the agreement between the Smagorinsky model and the SGS stress considerably. It also removed the need of prescribing the constant in the model and prescribed the correct near-wall behavior of the SGS viscosity. The dynamic procedure was used in constructing a number of dynamic SGS models which have proven to be successful.

Unfortunately, the dynamic model has been found to yield a prediction of intermittent SGS viscosity field, including a significant partition of negative values which is destabilizing in the simulations. This problem was solved in [22] and [39] using the procedure of averaging over directions of statistical homogeneity. The averaging procedure is usable in flow that contains direction(s) of homogeneity such as many two-dimensional flows such as channel flow, flow over a backward-facing step, flow over infinite cylinders etc. The absence of directions of homogeneity prevents the use of such averaging in the simulation of the flow around a three-dimensional bluff body such as a car. Other procedures for stabilizing the SGS viscosity field are proposed in [65] and [42] but they have not been used for complex flows where the intermittency in the SGS viscosity field is large.

My personal opinion is that the use of a simple Smagorinsky model in the LES of the flow around a car is probably sufficient. I motivate this statement with the small influence of the SGS model on the large-scale structures that dominate this flow.

Chapter 3

From a cube to a car

This section will describe my efforts to develop the LES for external vehicle aerodynamics. The choice of the test cases for the simulations was driven by the character of the flow and its similarity with the flow around a car, documentation of the flow, Reynolds number and the complexity in the geometry of the body. The shape of the body used in the simulations was chosen to be simple, allowing me to concentrate more on LES and less on the construction of the computational grid.

3.1 Flow around a cube

The first flow selected was that around the cube mounted on the wall of a wind tunnel at a Reynolds number of 40000 based on the incoming velocity and height of the cube. The experimental data for the time-averaged flow is reported in [38] ,[41] and [29] and the flow was simulated using both RANS and LES [25, 59, 55]. The points of similarity between this flow and that of the flow around a car are in the separations and re-attachments and several vortices that define the dynamics of the flow but, as shown later in the paper, there are also many differences.

This flow was computed in [55] using LES and gave good agreement with experimental data but, as noted in [34], the extension of such LES to the higher Reynolds number flow leads to very high computational costs. Simulations in [55] used instantaneous results of LES of channel flow as the inlet boundary condition and very fine computation grid. Thus my study of this flow aimed to investigate whether it can be simulated using a simple inlet boundary condition and coarse computational grid.

The separation on the front edges minimizes the influence of the upstream flow on the results downstream of the front face of the cube. Thus the experimental profile (constant in time) was used as the inlet condition in this work. The lateral boundaries were treated as slip surfaces using symmetry conditions $\partial\bar{u}/\partial z = \partial\bar{v}/\partial z = \bar{w} = 0$. At the downstream boundary, the convective boundary condition of $\partial\bar{u}_i/\partial t + U_c\,(\partial\bar{u}_i/\partial x) = 0$ was used. Here, U_c was set equal to the mean bulk velocity, U_b. No-slip conditions were used at the solid walls. The homogeneous Neumann condition was used for the pressure at all boundaries. The extent of the computational domain was, similar to the simulations in [55], three cube heights upstream of the cube, six cube heights downstream and seven cube heights laterally (see Fig. 3.1). The grid used in the simulations was four times smaller (0.27×10^6 cells) than the grids in [55]. The distance of the nearest grid point from the solid wall was $0.023H$, which is approximately two times the distance in the simulations in [55] (see [54]). The inadequate resolution is compensated for by the use of a dynamic one-equation SGS model. Two one-equation subgrid models, described in [12] and [44], are used to model the subgrid-scale stress tensor. Both models are subgrid-scale kinetic energy models. The SGS stress tensor is modeled as $\tau_{ij} = -2\nu_{sgs}\bar{S}_{ij}$ where the eddy viscosity is defined as $\nu_{sgs} = C\Delta k_{sgs}^{\frac{1}{2}}$ and SGS kinetic energy as $k_{sgs} = 1/2\tau_{ii}$. A detailed description of these models can be found in [34].

Figures 3.2 and 3.3 compare the time-averaged streamlines in the symmetry plane and in the plane near the wind tunnel wall, respectively, for two LES and experiments. Both simulations predicted the horseshoe vortex and the separation regions on the roof, lateral sides and behind the cube which are in agreement with the experiments (Figs. 3.2 and 3.3). The predicted separation lengths, X_{F1} and X_{R1} (Fig. 3.2c), differed $6-7\%$ and $14-16\%$, respectively, between my LES and the experiments. The same lengths were predicted in [55] within $1-29\%$ accuracy for X_{F1} and $7-13\%$ accuracy for X_{R1}. The main difference in the picture of the time-averaged flow between the experiment and LES is in the size and shape of the horseshoe vortex (Fig. 3.3). The separation between the two legs of this vortex at $0.75H$ downstream of the cube is larger by 36% than in the experiment. At $4.3H$ downstream of the cube, this difference decreased to only 2%. The difference in the location of the horseshoe legs was explained by findings of Martinuzzi and Tropea [41] that the shape of the horseshoe vortex is influenced by the oncoming boundary layer. Some differences were found in the

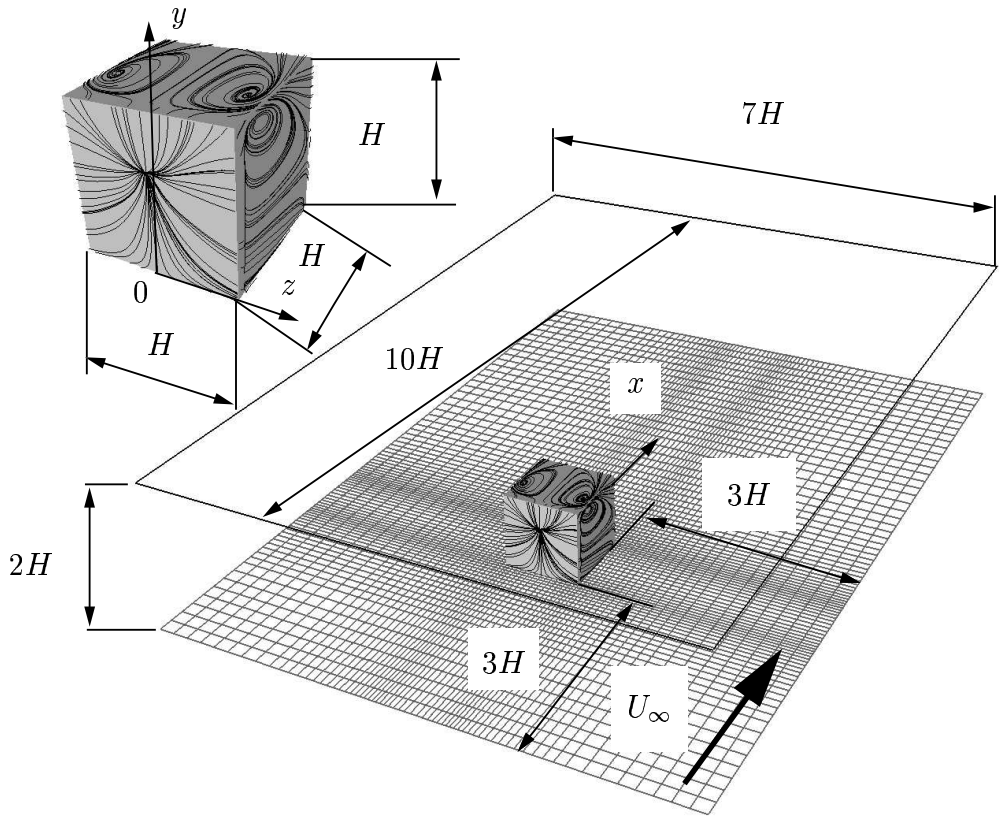

Figure 3.1: Geometry of a cube placed on a wind tunnel wall. Time-averaged trace lines are plotted on the surface of the body showing the roof and the lateral vortices. View of the front face of the cube.

predicted topology of the time-averaged flow between the two simulations (Fig. 3.3). The saddle points on the wind tunnel floor along the re-attachment line (S_2 in Fig. 3.3c) were predicted with the model from [44] whereas the model from [12] failed to do so. A comparison of the coherent structures of the time-averaged flow in experiments and LES is presented in Fig. 3.4. The horseshoe vortex, H, two lateral side vortices, L, the roof vortex, T, and the arch vortex, W, in the separation bubble behind the body are all accurately predicted in LES. The cores of these vortices are visualized in this figure using the critical point theory [11, 64], i.e. we plotted the points whose rate-of-deformation tensor has one real and a pair of complex-conjugate eigenvalues and whose velocity is zero.

The instantaneous flow (Fig. 3.5) differs from the time-averaged one.

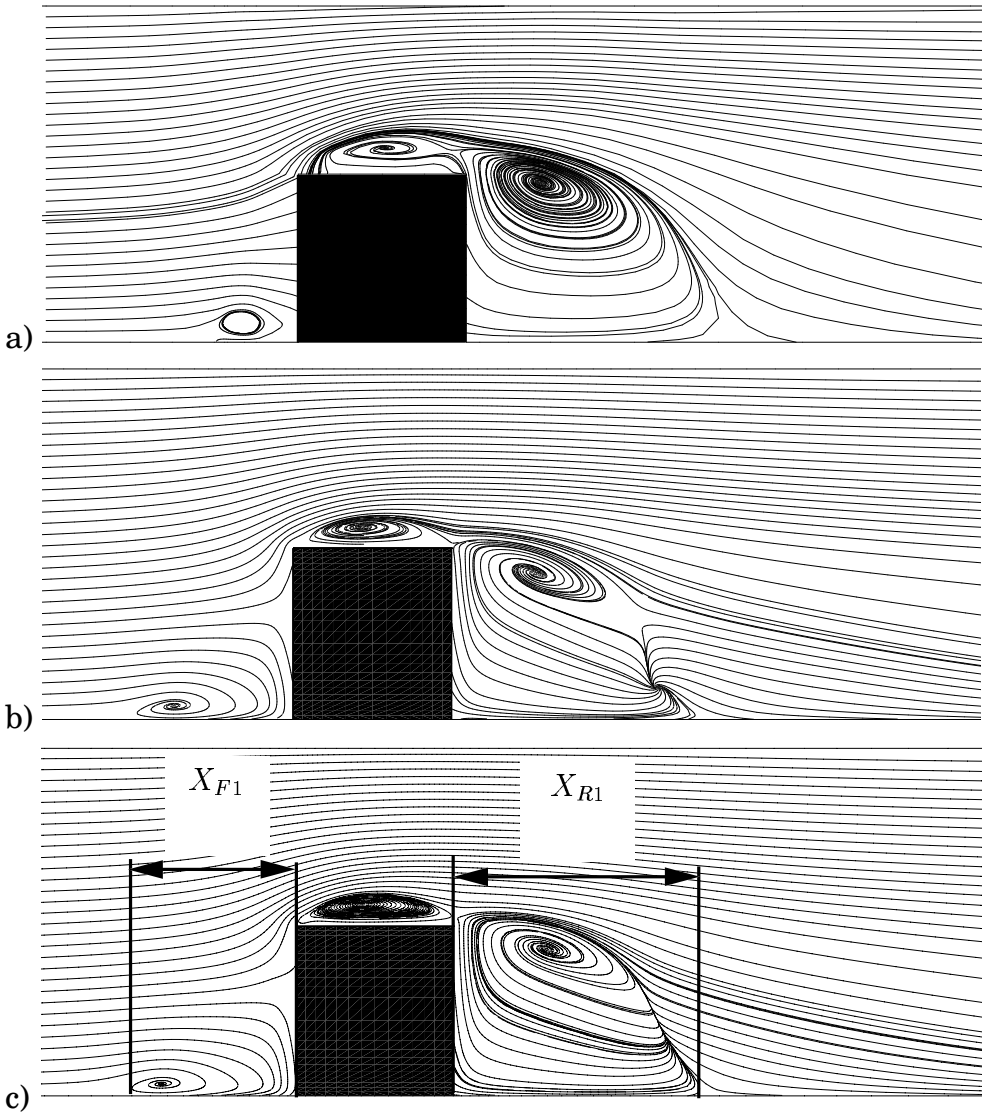

Figure 3.2: Streamlines of the mean flow projected onto the center plane of the cube using: a) experiment by Hussein and Martinuzzi [29]; b) model from [44]; c) model from [12] (note that the streamlines in Figs. b and c are emitted from the same positions in the flow.).

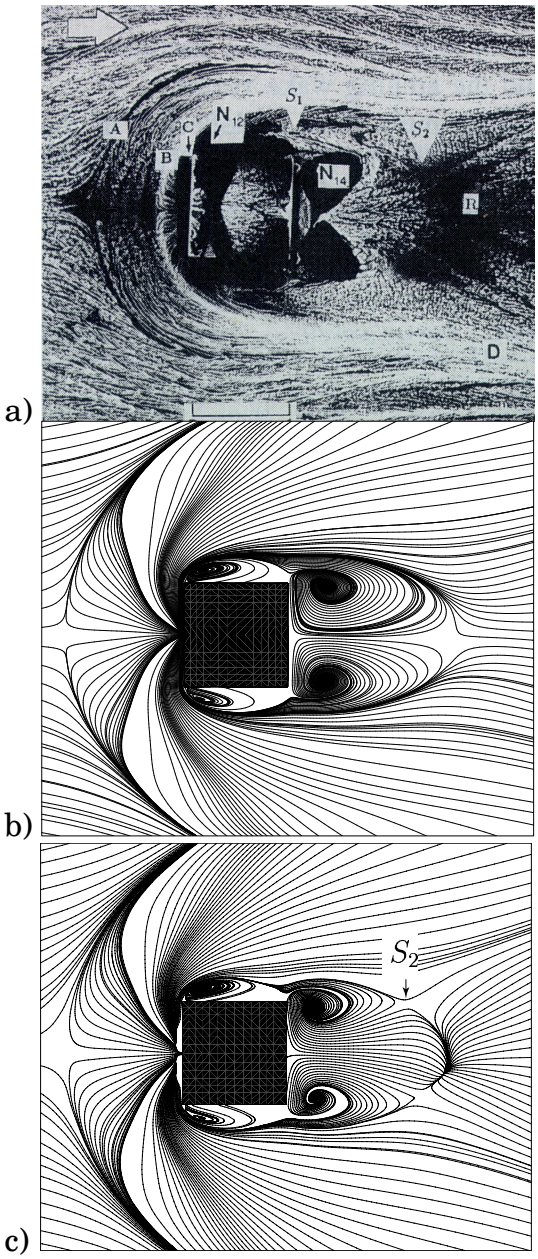

Figure 3.3: a) Oil-film visualization by Martinuzzi and Tropea (from [29] reproduced by permission of Physics of Fluids) compared with streamlines of the mean flow projected onto the wind tunnel floor for LES with b) model from [12] and c) model from [44] (note that the streamlines in Figs. b to c are emitted from the same positions in the flow.).

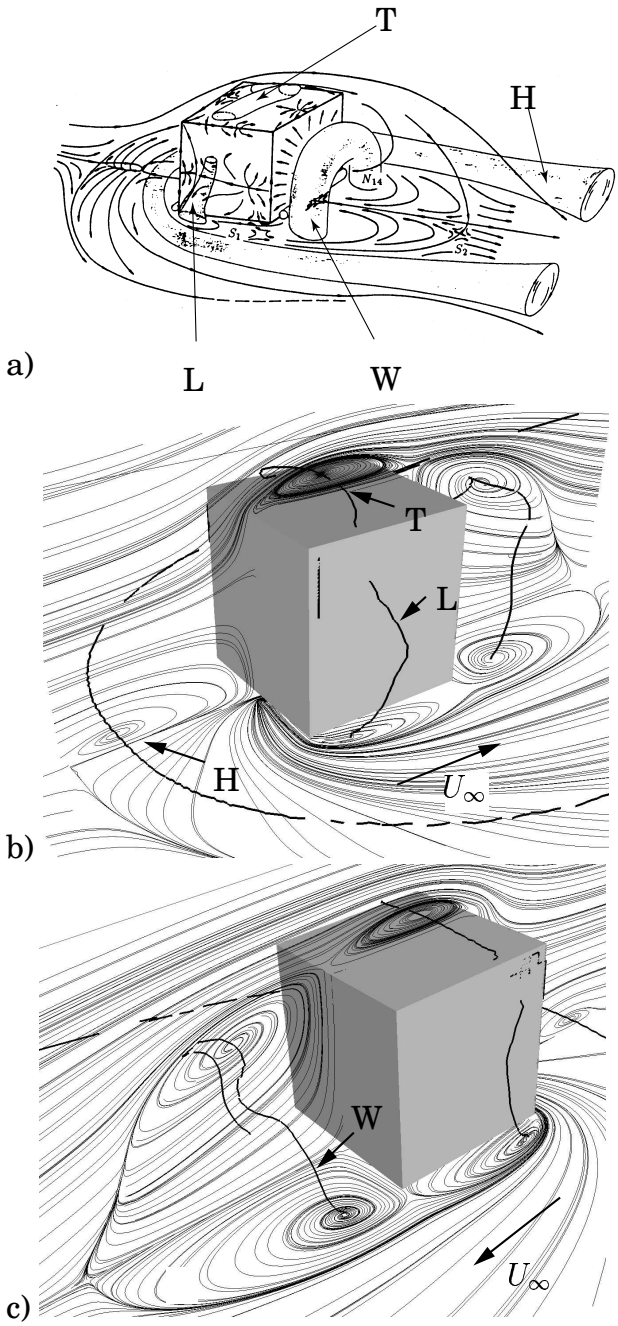

Figure 3.4: a) Schematic representation of the flow features by Martinuzzi and Tropea (from [29] by permission of Physics of Fluids). Time-averaged streamlines projected onto planes $x = 0$ and $z = 0$ in Figs. b and c. LES using model from [12]. The black curves represent the vortex cores. b) View of the front face of the body. c) View of the rear face of the body.

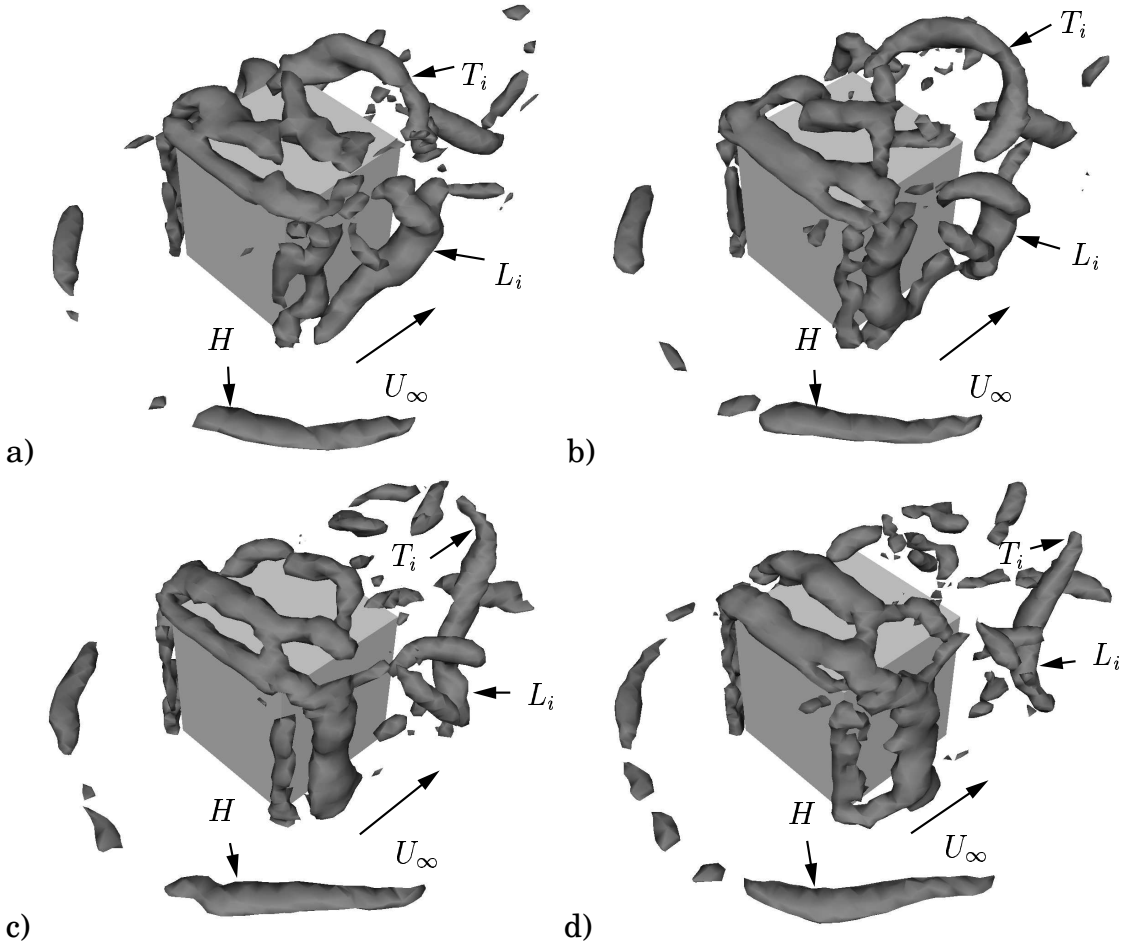

Figure 3.5: Instantaneous second invariant of the velocity gradient $Q = 5$. The time difference between the two pictures is $tU_\infty/H = 0.4$. View of the front face of the body.

The time-averaged vortices, L and T (Fig. 3.4), are averaged from a number of instantaneous vortices, L_i and T_i, respectively, in Fig. 3.5. The flow separates on the sharp front edges and forms instantaneous vortices T_i and L_i. As they are transported downstream, these vortices break down (Fig. 3.5c) and interact with each other. They produce fluctuating forces on the body. The side force signal was Fourier transformed, and a peak is found in the spectrum. The Strouhal number of this periodic component was found to be 0.134 as compared to the experimental value of 0.145. For comparison it can be mentioned that no shedding frequency was reported in previous LES [59] while the shedding period corresponding to a Strouhal number of 0.17 was observed

in the unsteady RANS simulation in [30].

The present simulations showed that LES using simple inlet boundary conditions, a relatively coarse grid and a one-equation SGS model gives accurate results. Although these results are encouraging, the conclusions of the feasibility of the LES of the flow around a car cannot be drawn from them owing to the difference in the flow and the geometry between the two flows. The car body is lifted from the floor and the flow coming from under the body makes the instantaneous wake longer than in the flow behind the cube. The position of the car body makes the wake more instantaneous with one additional degree of freedom (in the negative y direction). The absence of the sharp edges, such as those on a cube, on a car body can result in smaller regions of separated flow close to the front face of a car. Thus the influence of the upstream flow and thereby of the inlet boundary condition on the wake flow can be greater. Besides the physics of the flow, which is changed with the geometry of the body, the choice of the numerical method is also affected. The shape of the cube made it possible for me to use a single-block Cartesian code that was optimized for this kind of flow. The computation of the flow around a complex geometry car at higher Reynolds number (thus more cells) calls for the use of a code that is parallelized using block decomposition and PVM or MPI message passing systems such as that used in the next test case.

3.2 Flow around a simplified bus

A flow around a bus-shaped body [17, 18] was chosen as a second test case. This flow is similar to the flow around a real vehicle and some knowledge of this kind of flow is available from previous experimental and numerical studies [9, 2, 5, 18, 24]. As the flow is characterized by a fairly high Reynolds number (0.21×10^6, based on the model height H and the incoming velocity), the resulting flow features and the character of the flow-induced forces on the body should be similar to that in the flow around a full-scale vehicle. At the same time, the high Reynolds number implies high computational cost, as illustrated above.

The shape of the body is based on the Ahmed's body [2] and it is shown placed above the wind tunnel wall in Fig. 3.6. A computational domain with an upstream length of $8H$, a downstream length of $21H$ and a span-wise width of $5.92H$ was used for the simulations. A moving ground belt in the experiment [17, 18] was simulated in the simulations by applying the inlet velocity, U_∞, on the floor. The near-wall

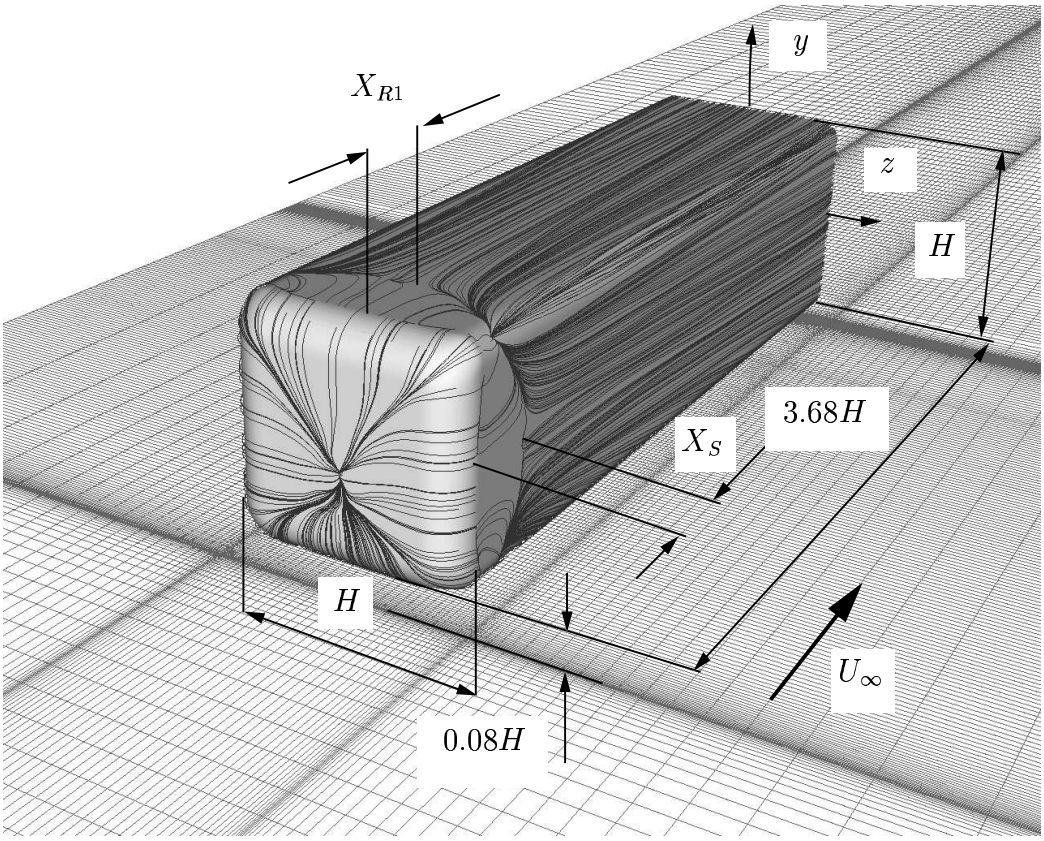

Figure 3.6: Geometry of the bus-shaped body placed above the wind tunnel wall. Time-averaged trace lines are plotted on the surface of the body showing the roof and the lateral vortices that extend X_{R1} and X_S, respectively, in the stream-wise direction.

spatial resolution expressed in the wall units was $\langle \Delta s^+ \rangle_t = 5-164$ in the stream-wise direction, $\langle \Delta n^+ \rangle_t = 0.5 - 0.8$ in the wall-normal direction and $\langle \Delta l^+ \rangle_t = 14 - 142$ in the span-wise direction. The no-slip boundary conditions were applied on the solid walls. The Smagorinsky model [60] for the SGS stress tensor was chosen for its simplicity and low computational cost.

The flow separates at the rounded side and roof edges of the body and forms transversal vortices (Fig. 3.7a) similar to Kelvin-Helmholtz vortices found on the Ahmed's body in [63]. These vortices are lifted further back, forming hairpin vortices in Fig. 3.7b. They average to three separation regions, shown in Fig. 3.8b. Two kinds of critical points [48] are visible in this figure. These are one unstable node Z (see also Fig. 3.9a) at the upper lateral edge of the bus and saddle points S_d (see also Fig. 3.9b) and S_s (see also Fig. 3.10a) downstream of separation regions R and L, respectively. Figure 3.8a shows the instantaneous trace lines on the surface of the body. There are no distinct separation or reattachment curves in the instantaneous flow (Fig. 3.8a) such as those that exist in the time-averaged flow (Fig. 3.8b).

It is shown in Figs. 3.9 and 3.10a that the critical point, Z, is an unstable node and that points S_d and S_s are saddle points. Attachment lines are shown in Figs. 3.9 and 3.10a . As can be seen in Fig. 3.11, the lateral vortices are attached to the under-body of the bus in focus F_c. Two counter-rotating longitudinal vortices (Fig. 3.12) are formed close to the unstable node, Z, in Fig. 3.8 and one longitudinal vortex (Fig. 3.13) is formed close to the unstable node, G (Fig. 3.11b), on each side of the bus. Similar longitudinal vortices on the roof of the body were observed in the experiment with the Ahmed's body flow [63] while the lower-edge longitudinal vortices were registered in a previous numerical study by Han [24]. The instantaneous wake region was found to consist of large-scale coherent structures with their axes parallel to the separation edges on the rear face of the body. These structures average to the vortex ring [37, 36] in agreement with experimental observations [17, 18, 2]. Besides this large vortex, four thin vortices (B in Figs. 3.14 and 3.17) were observed close to the rear edges. Two of these vortices (the upper-edge and the lower-edge vortices) are shown in Figs. 3.14b and c and one vortex in plane $y = 0$ is shown in Fig. 3.17. Figures 3.14b and c show that the direction of rotation of the upper-edge and lower-edge vortices is counter-clockwise and clockwise, respectively. Six half-saddles (S_4-S_9) and two foci (N_2 and N_3) are visible in Fig. 3.14. The stream-wise length of the separation bubble in Fig. 3.14a, X_r was overpredicted by some 7% compared to experiments

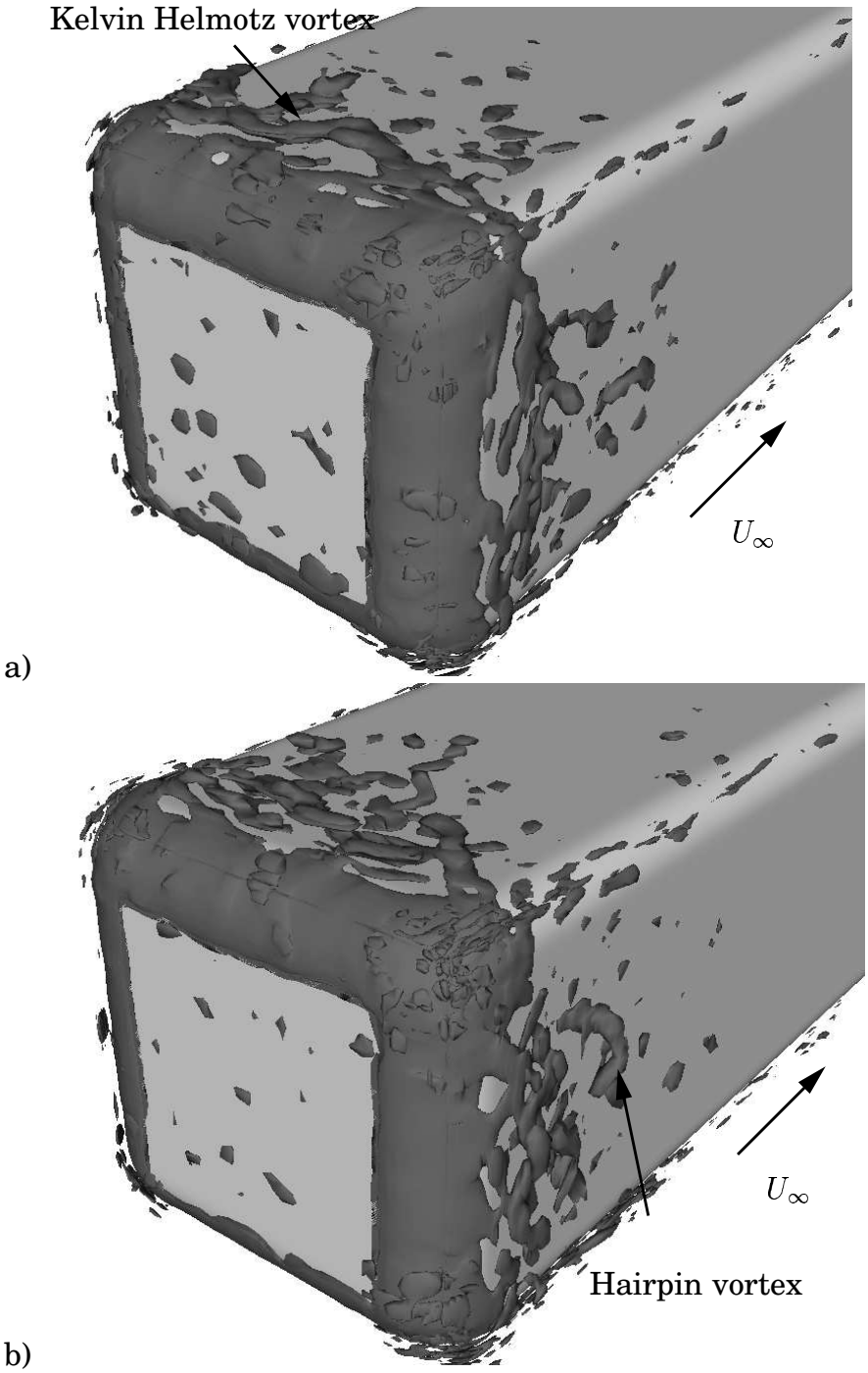

Figure 3.7: Instantaneous vortices formed after the separation on the front edges of the body. Isosurface of second invariant of the velocity gradient $Q = 8000$. The time difference between the two pictures is $tU_\infty/H = 0.8$.

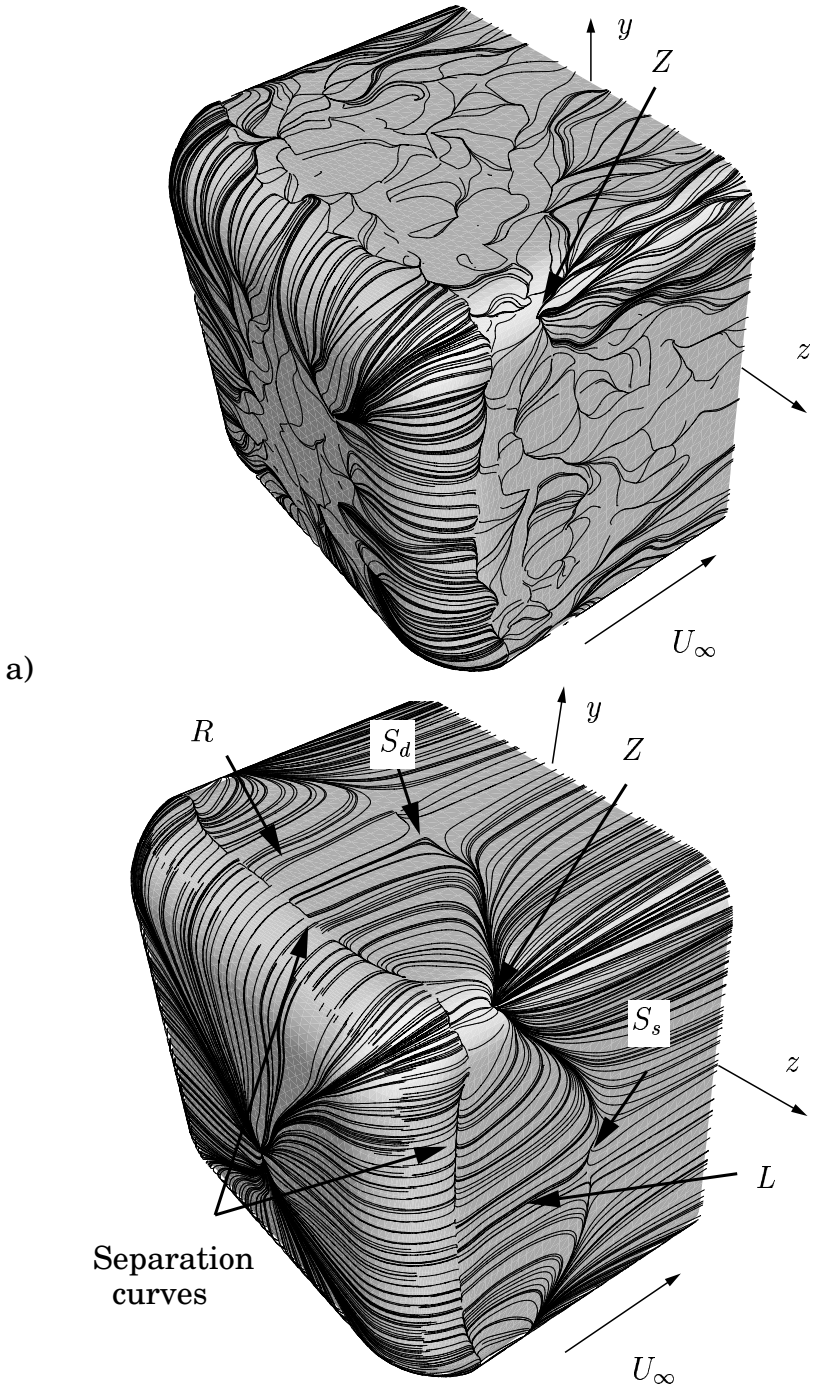

Figure 3.8: a) Instantaneous trace lines on the surface of the body. b) Time-averaged trace lines on the surface of the body showing the roof vortex, R, and the lateral vortex, L. View of the front face of the body.

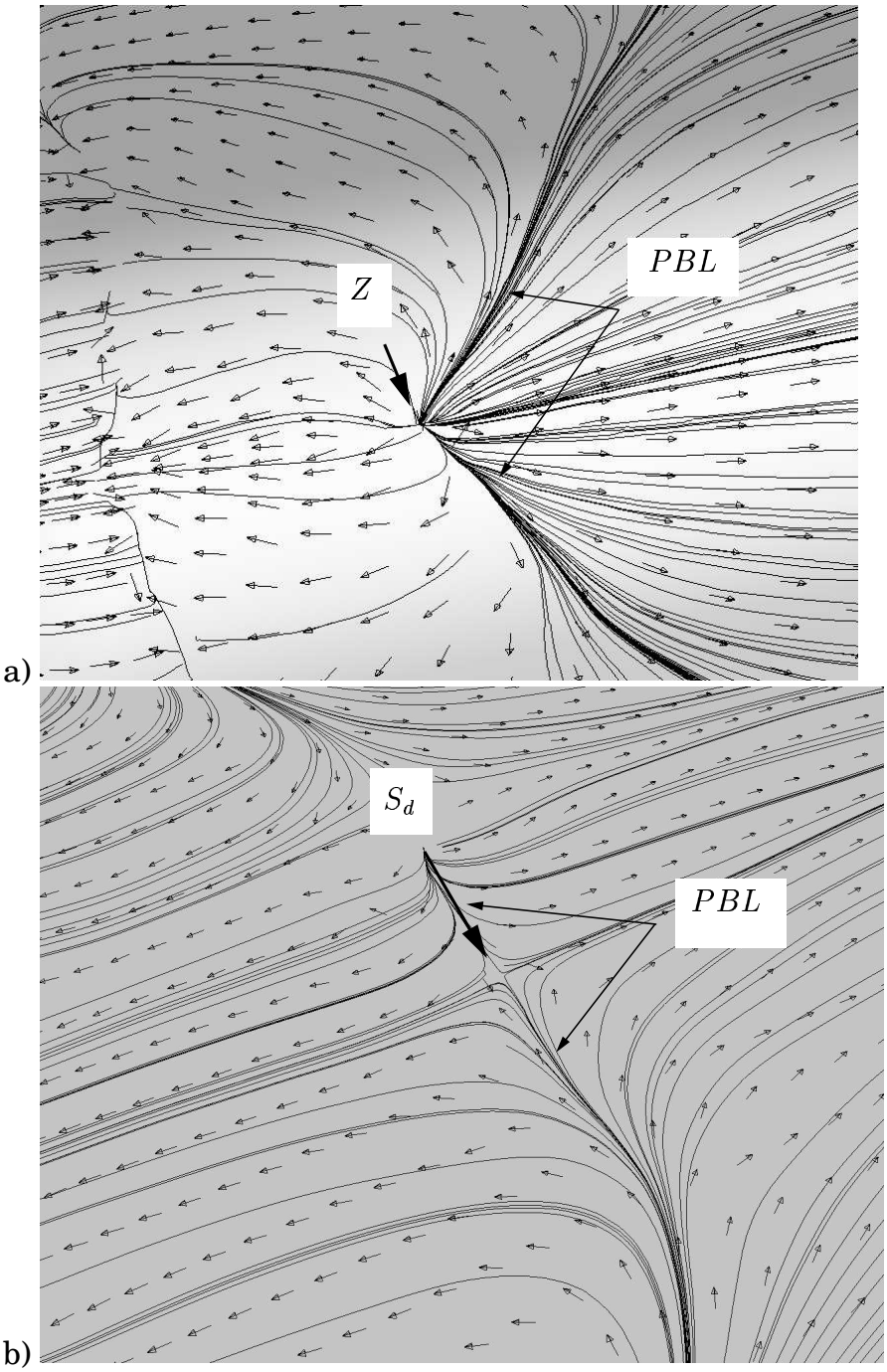

Figure 3.9: Time-averaged trace lines on the surface of the body showing the unstable node, Z, and the saddle points, S_d, downstream of the separation region, R. PBL are attachment lines. The velocity vectors are plotted at the surface parallel to the body surface at the wall-normal distance of $1.6 \times 10^{-4} H$.

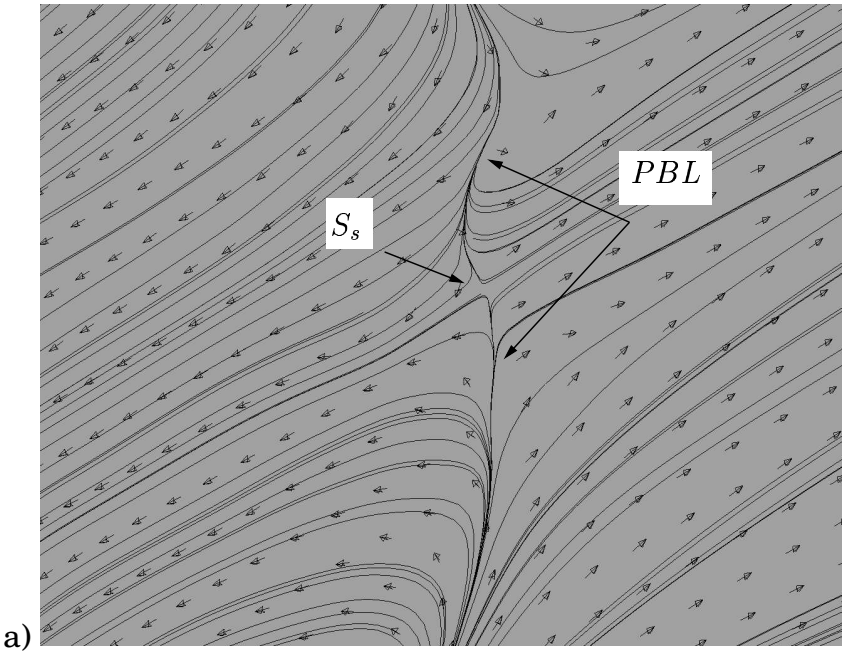

a)

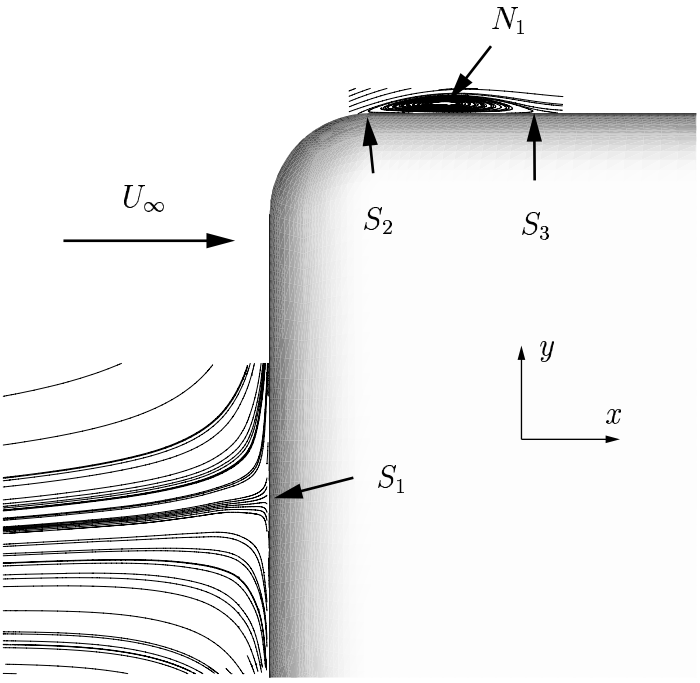

b)

Figure 3.10: a) Time-averaged trace lines on the surface of the body showing the saddle point, S_s, downstream of the separation region, L. PBL are attachment lines. The velocity vectors are plotted at the surface parallel to the body surface at the wall-normal distance of $1.6 \times 10^{-4} H$. b) Time-averaged streamlines projected onto symmetry plane $z = 0$ showing half-saddles S_1, S_2 and S_3 and focus N.

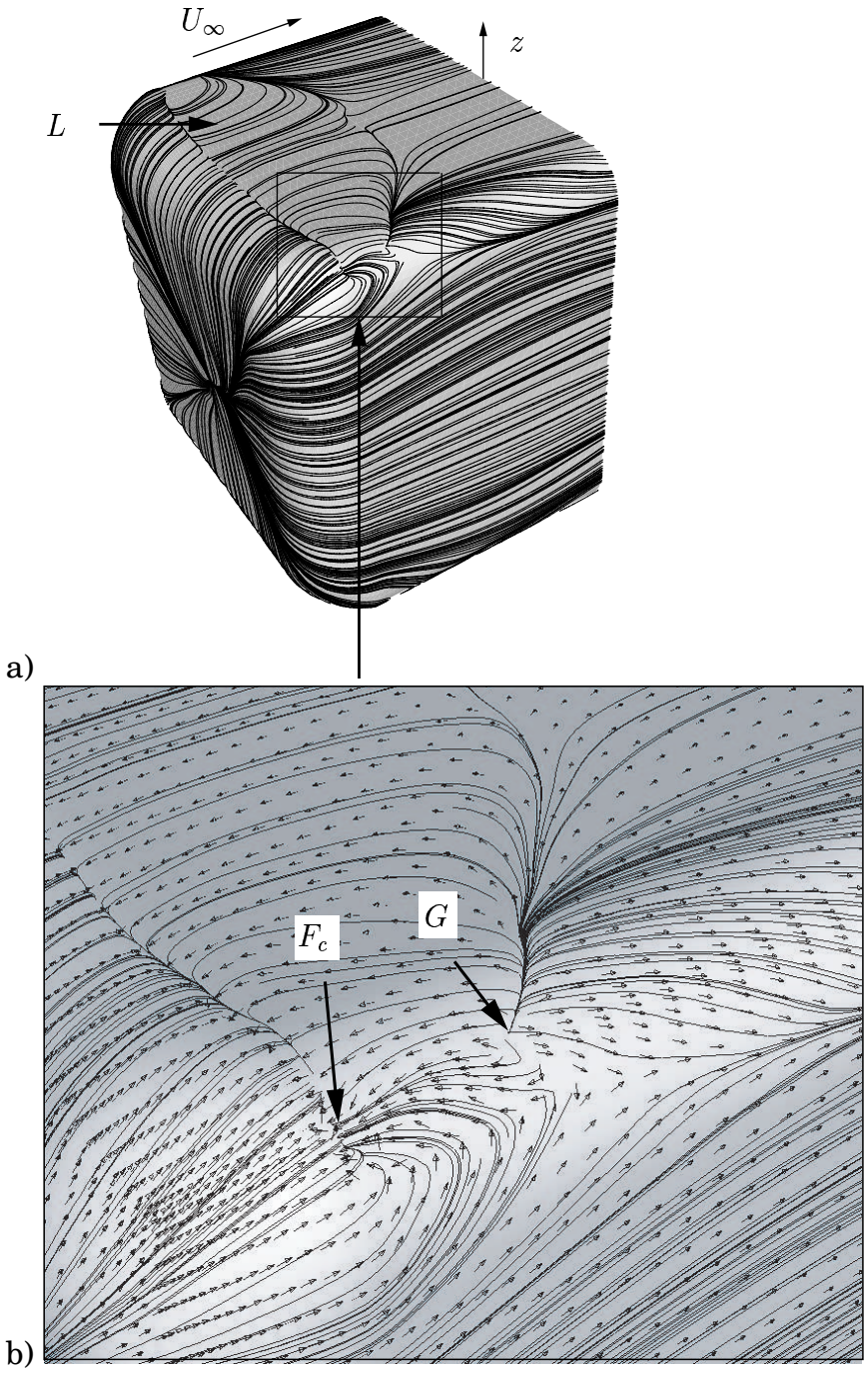

Figure 3.11: a) Time-averaged trace lines on the surface of the body. View from below. b) Zoom of Fig. a. The velocity vectors are plotted at the surface parallel to the body surface at wall-normal distance of $1.6 \times 10^{-4} H$. F_c is a focus and G is an unsteady node [48].

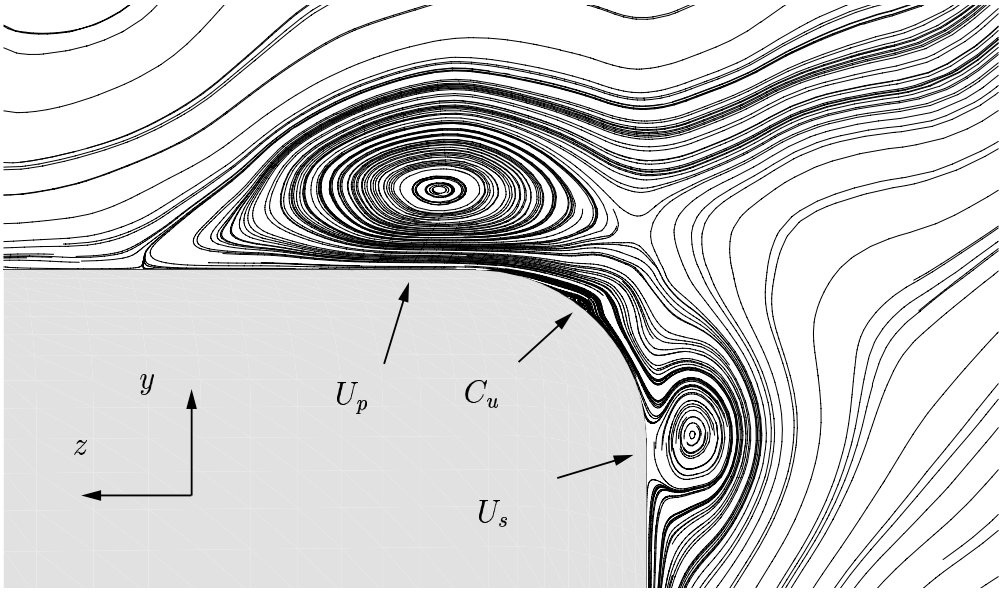

Figure 3.12: Time-averaged streamlines projected onto plane $x = -1.28H$. The rotation of U_p and U_s is counter-clockwise and clockwise, respectively. View from behind the upper-right edge of the body.

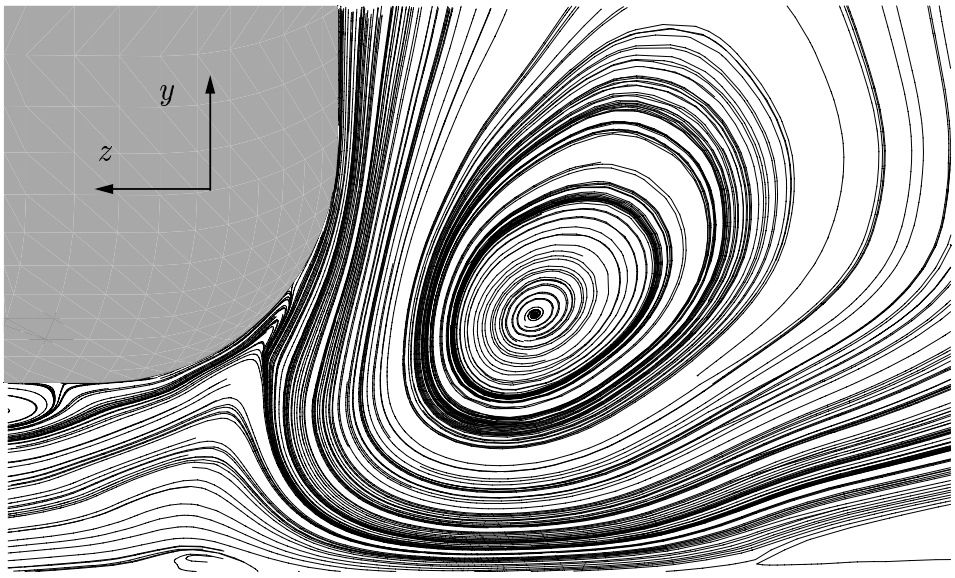

Figure 3.13: Time-averaged streamlines projected onto plane $x = -0.48H$. The direction of the rotation of this vortex is counter-clockwise. View from behind the lower-right edge of the body.

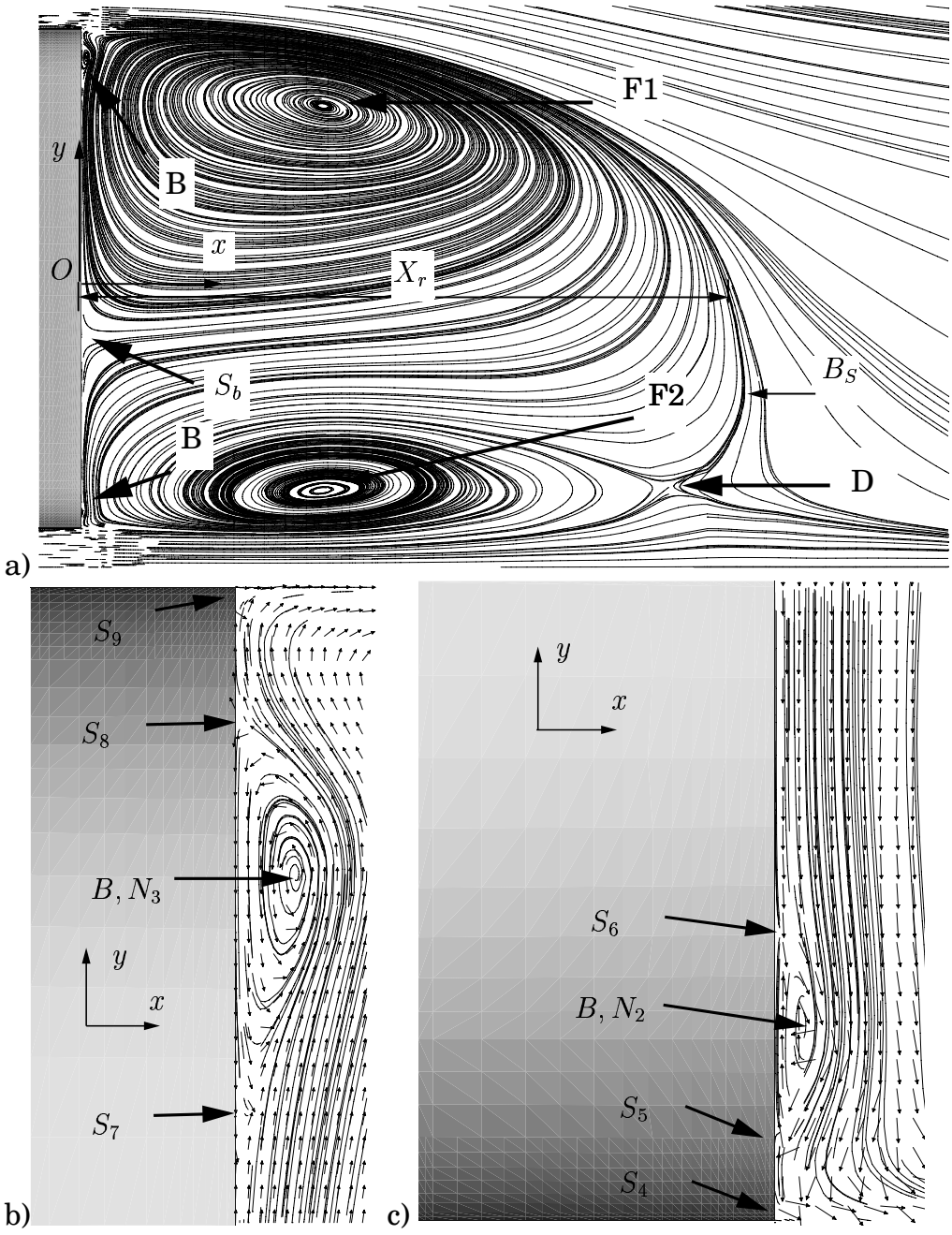

Figure 3.14: a) Time-averaged streamlines projected onto symmetry plane $z = 0$ of the bus. S_b is the stagnation point on the rear face of the bus, B_S is the free stagnation point, D is the saddle point and F1 and F2 are foci of the upper and lower vortices, respectively. b) upper-edge thin vortex B. c) lower-edge thin vortex B.

[17, 18]. This was explained in [36] by a somewhat coarse computational grid in the span-wise direction and experimental uncertainty.

Figure 3.15 shows the upper and the lower longitudinal edges of the body. The streamlines and the velocity vectors projected on the surface show that there is one separation line close to the lower longitudinal edge (Fig. 3.15b) and no separation or re-attachment line close to the upper longitudinal edge (Fig. 3.15a). Figures 3.16 and 3.19 sketch the time-averaged flow patterns and the critical points from Figs. 3.10 and 3.14 and Figs. 3.17 and 3.18 in two symmetry planes of the bus ($y = 0$ and $z = 0$). According to Hunt *et al.* [28], there can only be a certain number of saddle points for a given number of nodes. They derived a relation for a two-dimensional section of the flow

$$\left(\sum\nolimits_N + \frac{1}{2}\sum\nolimits_{N'}\right) - \left(\sum\nolimits_S + \frac{1}{2}\sum\nolimits_{S'}\right) = 1 - n \tag{3.1}$$

where $\sum_N$ is the number of nodes and foci, $\sum_{N'}$ is the number of half-nodes (nodes on the boundaries), $\sum_S$ is the number of saddles and $\sum_{S'}$ is the number of half-saddles. n is the connectedness of the surface. For a singly connected region, with no body, $n = 1$; with one body (as in our case) $n = 2$ etc. Let us now investigate whether the critical points in Figs. 3.16 and 3.19 satisfy the topological constraint in Eq. 3.1. In Fig. 3.16 $\sum_N = 5$, $\sum_{N'} = 0$, $\sum_S = 1$ and $\sum_{S'} = 10$ so that $(\sum_N + 1/2\sum_{N'}) - (\sum_S + 1/2\sum_{S'}) = 5 - (1 + 5) = -1$ and in Fig. 3.19 $\sum_N = 6$, $\sum_{N'} = 0$, $\sum_S = 1$ and $\sum_{S'} = 12$ so that $(\sum_N + 1/2\sum_{N'}) - (\sum_S + 1/2\sum_{S'}) = 6 - (1 + 6) = -1$. This agrees with Eq. 3.1, since $n = 2$. Thus these figures represent a flow that is kinematically possible. After the closure of the bubble, a pair of the counter-rotating longitudinal vortices was observed in the time-averaged flow in agreement with the experimental observations of similar flows [1, 2, 5, 7]. The observation of Bearman [7] that the instantaneous vortices are very different from the coherent structures that appear in the instantaneous flow was confirmed in this simulation (see [36]). For additional details on the flow features and the mechanisms of their origin, I refer to [36]. It should suffice to say here that the LES gave accurate representations of the coherent structures in this flow and explained their formation and interaction.

Now we shall consider the ability of LES to predict the aerodynamic forces and their variation. In the absence of experimental data from experiments in [17] and [18], the time-averaged drag and lift coefficients were compared with those in experiments by Barlow *et al.* [6] for a similar body. Note that the floor in the experiment by Barlow *et al.* [6]

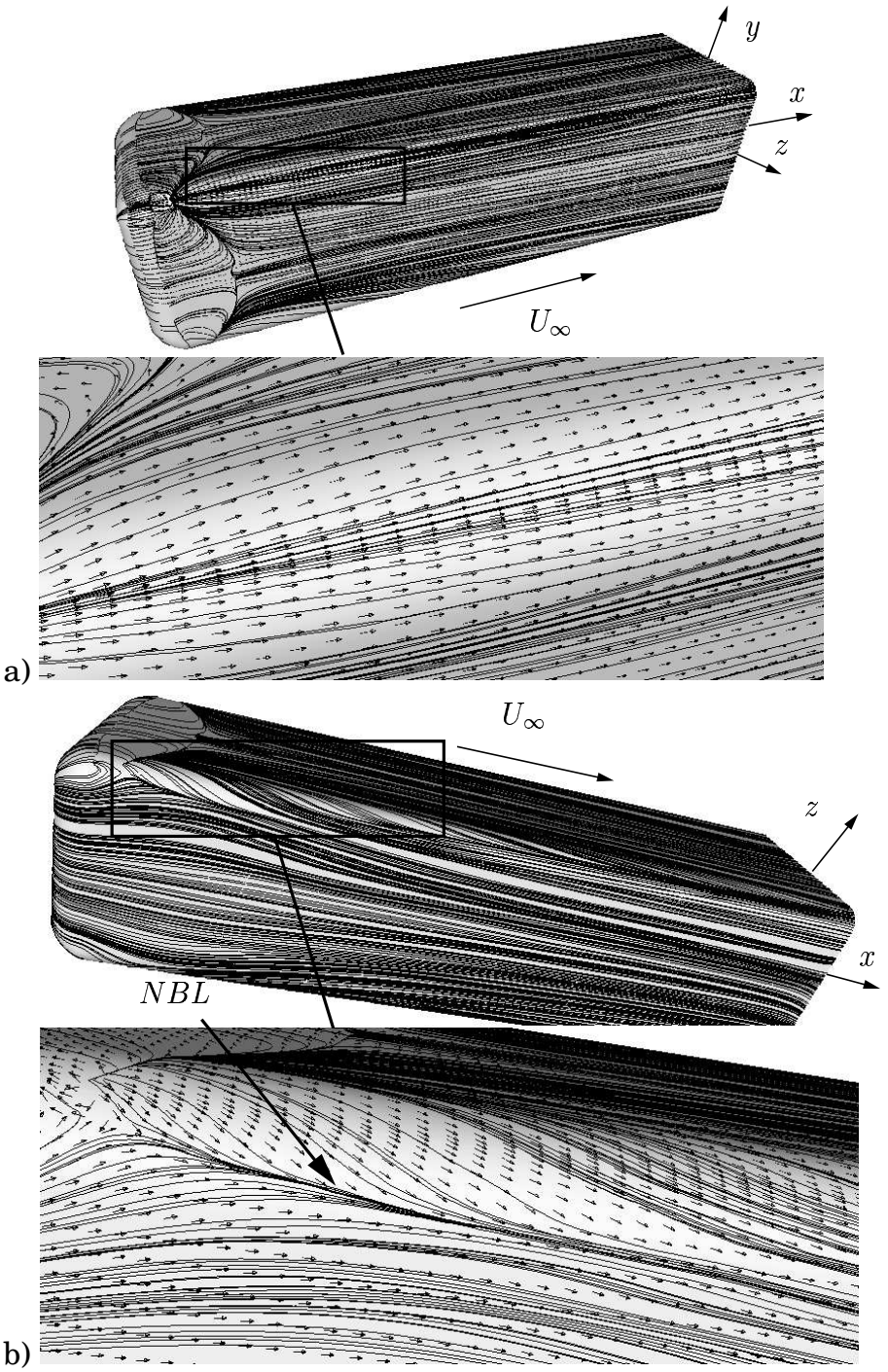

Figure 3.15: Time-averaged trace lines on the surface of the body. a) View of the upper lateral edge. b) View of the lower lateral edge. NBL is the separation line. The velocity vectors are plotted at the surface parallel to the body surface at the wall-normal distance of $1.6 \times 10^{-4} H$.

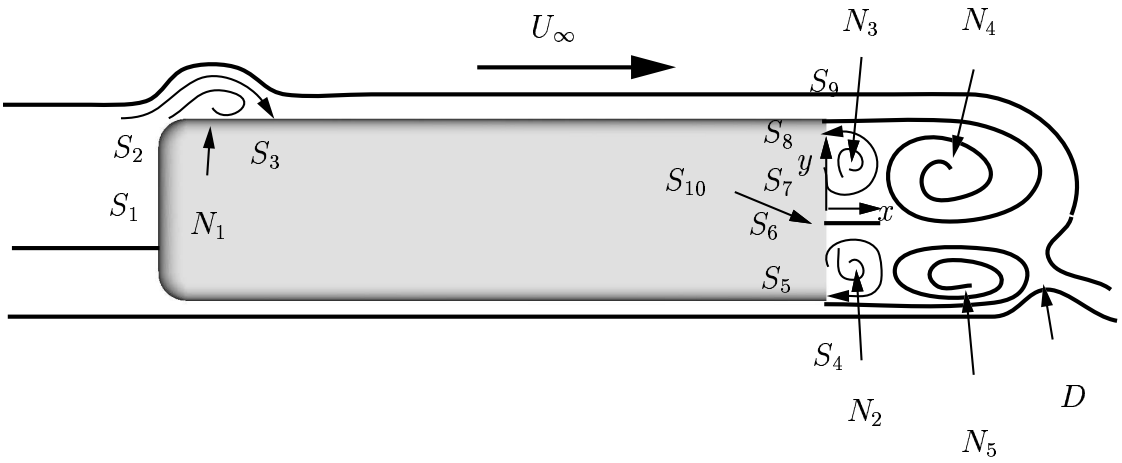

Figure 3.16: Schematic representation of time-averaged streamlines and singular points on the symmetry plane, $z = 0$, of the bus. S_1-S_{10} are half-saddles, N_1-N_5 are foci and D is the saddle point.

was stationary, unlike the moving floor in the experiment by Duell and George [18], and it is known (see [8]) that the moving floor influences the flow. (For example, Bearman *et al.* [8] found that floor movement reduces drag by 8% and lift by 30% in a case of a $1/3$rd scale car model.) The drag coefficient was found to be identical to the one in [6], whereas the lift coefficient was underpredicted by some 8%. The signals of the forces acting on the bus were Fourier transformed, and two main frequencies at Strouhal numbers 0.22 and 0.6 were observed in the side force signal, of which 0.22 is close to the shedding frequency of 0.23 found in Bearman's experimental study of the wake behind a car model [7]. The value of the pressure coefficient integrated over the rear face of the bus, for which experimental data exist from [17] and [18], was overpredicted in my LES by 5% of the dynamic pressure. This can be explained by the boundary layers that exist in the experiment on the side walls of the wind tunnel, which in the simulations were not resolved but replaced with slip conditions. More results on the transient forces, velocities and stresses can be found in [36].

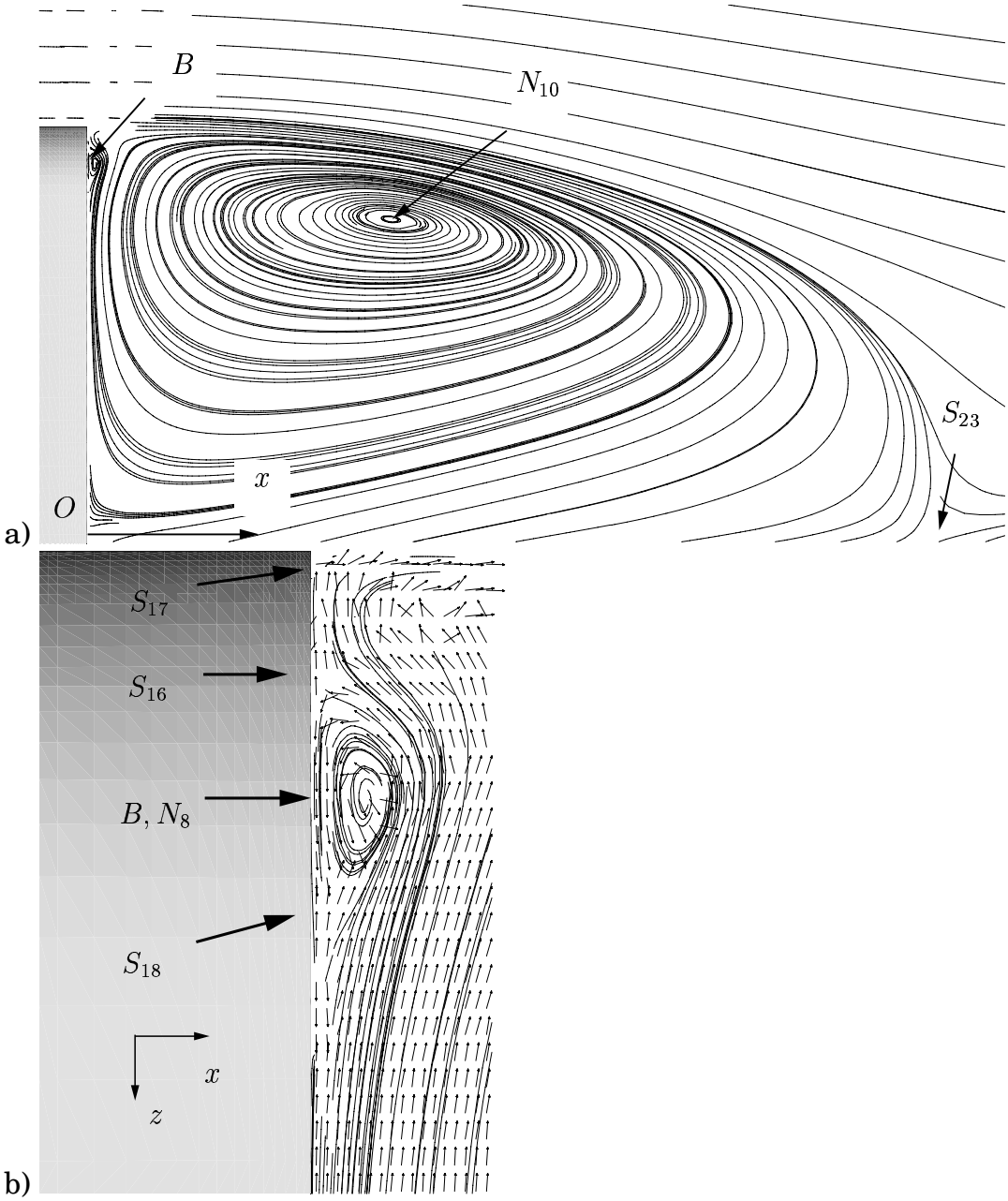

Figure 3.17: a) Time-averaged streamlines projected onto plane $y = 0$. N_{10} is foci and S_{23} is saddle point. b) Zoom of the lateral-edge thin vortex, B, for $z > 0$. S_{16}-S_{18} are half-saddles and N_8 is focus.

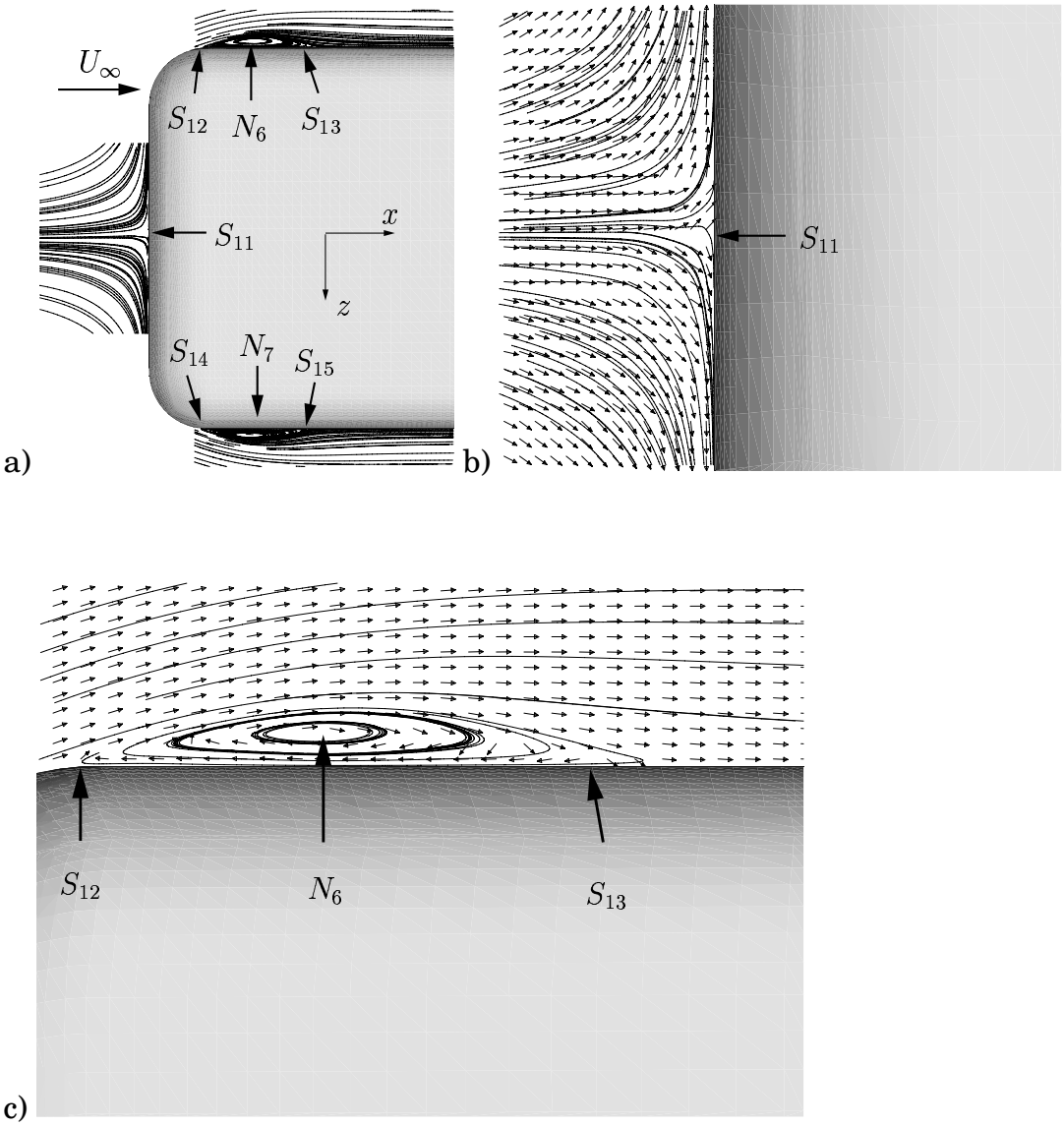

Figure 3.18: a) Schematic representation of time-averaged streamlines projected onto plane $y = 0$ showing half-saddles S_{11}-S_{15} and foci N_6 and N_7. b) Zoom of the stagnation point (half-saddle S_{11}). c) Zoom of the lateral side vortex.

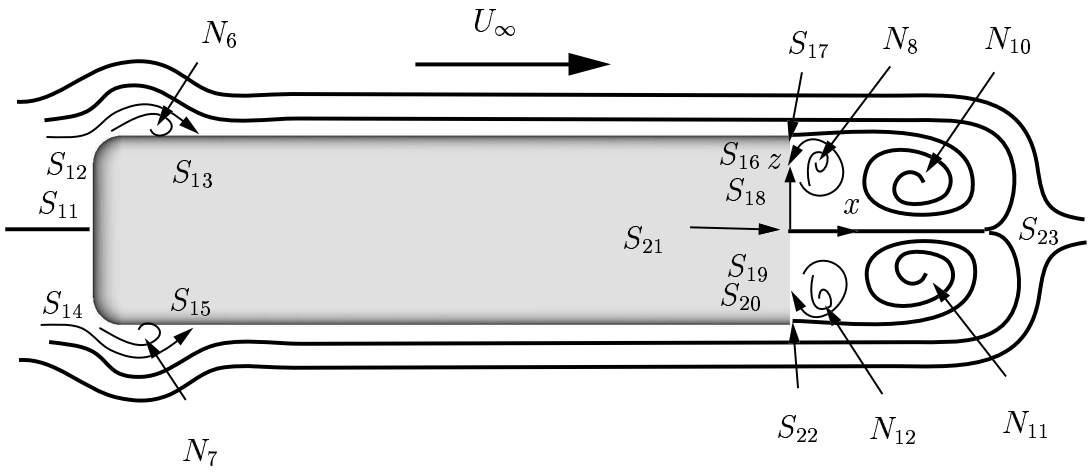

Figure 3.19: Time-averaged streamlines and singular points on the plane $y = 0$. S_{11}-S_{22} are half-saddles, N_6-N_{12} are foci and S_{23} is the saddle point.

Chapter 4

Perspectives on LES for vehicle aerodynamics

The conclusion drawn from the work reported in this thesis is that the near future of LES in vehicle aerodynamics is in the exploration of the physics of such flows. Making LES of the flow around vehicle models at lower Reynolds number, such as the simulation presented in this paper, is likely to be most useful. The strength of LES is that the transient processes can be studied in detail, which is difficult in experiments and impossible in RANS. Similar to DNS used to gain fundamental knowledge on turbulence physics, LES will be used to obtain the fundamental knowledge of a car's flow physics. The idea is to use this understanding of the flow at lower (LES feasible) Reynolds number in modeling the flow at actual Reynolds numbers and as an aid for the stylist in improving aerodynamic properties when designing the car.

Although the commercial codes have begun to include LES models, the use of LES in external vehicle aerodynamics of full-size vehicles will be limited to qualitative understanding of the flow around small parts of vehicles such as mirrors. The automotive industry will continue (at least in the next decade) to rely on experimental studies for quantitative aerodynamic data such as drag and lift coefficients. Computational fluid dynamics (CFD) will not be used to predict the forces and moments acting on a car but to explain the reasons for them and to establish the outlines for their controlled change (by the stylist).

As computer power increases, higher Reynolds number (Re) flow around a car can be simulated using LES; however, reaching $Re = 5 \times 10^6$ requires an alternative simulation technique for the near-wall region that necessarily includes a certain amount of empiricism. Several hybrid methods entitled hybrid LES/RANS [15] methods or detached-

eddy simulation (DES) [62] are suggested, where the boundary layer (or a part of it) is modeled using RANS (in transient mode) and the separated flow away from the wall is simulated with LES. Many unresolved issues, such as the optimal position of the matching line between LES and RANS in hybrid LES/RANS, the choice of the RANS turbulence model or construction of the suitable computational grid, remain before these hybrid methods can be used for complex flow simulations.

Until an efficient and accurate way to model near-wall mechanisms is found, LES will be used in vehicle aerodynamics as a powerful complement to the experiments that enable us to understand this complex flow.

Chapter 5

Governing equations and the method

This section presents the numerical method used in this work. The governing LES equations and the subgrid-scale models used in the simulations are given. This is followed by a presentation of the two numerical methods used here to solve discretized equations.

5.1 Governing equation

The governing LES equations are the incompressible Navier-Stokes and the continuity equations filtered with a spatial filter of characteristic width, Δ (Δ is the grid resolution in this work):

$$\frac{\partial \bar{u}_i}{\partial t} + \frac{\partial}{\partial x_j}\left(\bar{u}_i \bar{u}_j\right) = -\frac{1}{\rho}\frac{\partial \bar{p}}{\partial x_i} + \nu \frac{\partial^2 \bar{u}_i}{\partial x_j \partial x_j} - \frac{\partial \tau_{ij}}{\partial x_j} \tag{5.1}$$

and

$$\frac{\partial \bar{u}_i}{\partial x_i} = 0. \tag{5.2}$$

Here, $\bar{u}_i$ and $\bar{p}_i$ are the resolved velocity components and pressure, respectively, and the bar over the variable denotes filtering. The filtering decomposes the fluid motion into a large-scale component that can be computed exactly and the small subgrid scale (SGS). This is done by applying a filtering operation

$$\bar{f}(x_i) = \int_\Omega f(x_i') G(x_i, x_i') dx_i' \tag{5.3}$$

where G is the filter function and Ω is the entire flow domain. A top hat filter with the filter function $G = \frac{1}{\Delta} H(\frac{1}{2}\Delta - |x - x'|)$, where $H(x)$ is the Heaviside function, is used in this work. The filter width, Δ, is defined as $\Delta = (\Delta_1 \Delta_2 \Delta_3)^{1/3}$ where Δ_i are the computational mesh sizes in each coordinate directions. The influence of the small scales of the turbulence on the large energy carrying scales in Eq. (5.1) appears in the SGS stress tensor, $\tau_{ij} = \overline{u_i u_j} - \bar{u}_i \bar{u}_j$, which must be modeled.

A large number of models for the SGS stress tensor have been proposed in the past four decades (see [43] for a review), most of them built on the algebraic eddy viscosity model originally proposed by Smagorinsky [60]. Four different SGS models were used in this work, of which three were dynamic one-equation models and the fourth was the Smagorinsky model [60]. The Smagorinsky model is used in the simulations of the flow around a bus and it represents the anisotropic part of the SGS stress tensor, τ_{ij}, as:

$$\tau_{ij} - \frac{1}{3}\delta_{ij}\tau_{kk} = -2\nu_{sgs}\bar{S}_{ij} \tag{5.4}$$

where $\nu_{sgs} = (C_s\Delta)^2|\bar{S}|$ is the SGS viscosity,

$$\bar{S}_{ij} = \frac{1}{2}\left(\frac{\partial \bar{u}_i}{\partial x_j} + \frac{\partial \bar{u}_j}{\partial x_i}\right) \tag{5.5}$$

is the resolved rate-of-strain tensor and $|\bar{S}| = \left(2\bar{S}_{ij}\bar{S}_{ij}\right)^{\frac{1}{2}}$. The Smagorinsky constant, C_s, must be adjusted for different flows. A value of $C_s = 0.1$ is used in this work.

One-equation models were used for the channel flow simulations and for the simulations of the flow around a cube. Two of the one-equation models were eddy viscosity models [12, 44]. One model [35], which was developed as a part of this project, was a mixed one-equation model. The eddy viscosity one-equation models use $k_{sgs}^{1/2}$ as the velocity scale and model the SGS stress tensor as $\tau_{ij} = -2C\Delta k_{sgs}^{1/2}\bar{S}_{ij}$ with the SGS kinetic energy defined as $k_{sgs} = 1/2\tau_{ii}$. In addition to the eddy viscosity part, the mixed one-equation model [35] has one scale similarity part (see [35]). For further details on these models, see [34] and [35].

5.2 Numerical methods

LES Eqs. (5.1) and (5.2) are discretized using a 3D finite volume method for solving the incompressible Navier-Stokes equations using a

collocated grid arrangement [14]. Both convective and viscous plus subgrid fluxes are approximated by central differences of second-order accuracy. The time integration is done using the Crank-Nicolson second-order scheme.

Two different computational codes were used. A single block code was used for the simulations of the flow around a cube and the channel flow simulations. The code is based on an implicit, two-step time-advancement method. The discrete form of Eq. 5.1 can be written as

$$\bar{u}_i^{n+1/2} = \bar{u}_i^n + \Delta t H(\bar{u}_i^n, \bar{u}_i^{n+1/2}) - \frac{1}{\rho}\alpha\Delta t\frac{\partial \bar{p}^{n+1}}{\partial x_i} - \frac{1}{\rho}(1-\alpha)\Delta t\frac{\partial \bar{p}^{n}}{\partial x_i} \quad (5.6)$$

where $H(\bar{u}_i^n, \bar{u}_i^{n+1/2})$ includes convection and the viscous and subgrid stresses and $\alpha = 0.5$ (Crank-Nicolson). Equation 5.6 gives $\bar{u}_i^{n+1/2}$, which does not satisfy continuity. An intermediate velocity field is computed by subtracting the implicit part of the pressure gradient, i.e.

$$\bar{u}_i^{*} = \bar{u}_i^{n+1/2} + \frac{1}{\rho}\alpha\Delta t\frac{\partial \bar{p}^{n+1}}{\partial x_i}. \quad (5.7)$$

Now $\bar{u}_i^{n+1/2}$ in Eq. 5.7 is replaced by the final velocity field at level $n+1$, i.e. $\bar{u}_i^{n+1}$. Taking the divergence of Eq. 5.7, and imposing the requirement that the face velocities $\bar{u}_{i,f}^{n+1}$ (which are obtained by linear interpolation) satisfy the continuity equation, the following is obtained

$$\frac{\partial^2 \bar{p}^{n+1}}{\partial x_i \partial x_i} = \frac{\rho}{\Delta t\alpha}\frac{\partial \bar{u}_{i,f}^{*}}{\partial x_i}. \quad (5.8)$$

The numerical procedure at each time step can be summarized as follows:

1. Solve the discretized filtered Navier-Stokes equation for $\bar{u}$, $\bar{v}$ and $\bar{w}$ using a symmetric Gauss-Seidel.

2. Create an intermediate velocity field, $\bar{u}_i^{*}$, from Eq. 5.7.

3. The Poisson equation (Eq. 5.8) is solved with an efficient multigrid method [19].

4. Compute the face velocities $\bar{u}_{i,f}^{n+1}$ (which satisfy continuity) from the pressure and the intermediate velocity as

$$\bar{u}_{i,f}^{n+1} = \bar{u}_{i,f}^{*} - \frac{1}{\rho}\alpha\Delta t\left(\frac{\partial \bar{p}^{n+1}}{\partial x_i}\right)_f. \quad (5.9)$$

5. Steps 1 to 4 are followed until convergence (normally one to three iterations) is reached.

6. The turbulent viscosity is computed.

7. Next time step.

Note that although no explicit dissipation is added to prevent odd-even decoupling, an implicit dissipation is present. The intermediate velocity field is computed at the *nodes* (see Eq. 5.7) by subtracting a pressure gradient. Then, after having solved the pressure Poisson equation, the face velocity field is computed adding a pressure gradient at the *faces* (see Eq. 5.9). Thus a term is added, which is the difference between the pressure gradient at the face and the node. It can readily be shown that this term is proportional to the third derivative of pressure, i.e. $\partial^3 p/\partial x_i^3$. This term corresponds to Rhie-Chow dissipation [52].

A multi-block version of the code [14] is used for the simulations of the flow around the bus. It uses the SIMPLEC algorithm for the pressure-velocity coupling. The code is parallelized using block decomposition and the PVM and MPI message passing systems [47]. Additional details on this code can be found in [46].

Chapter 6

Summary of papers

This section summarizes the papers attached in the thesis that consist the basis of this thesis. The papers are presented in chronological order. For each, a brief motivation and background are given, which are followed by my work and the results. Three main topics were considered in these papers. The flow around a cube is discussed in Papers I-IV and VII. Papers V, VI, IX and X consider flow around a simplified bus and in Paper VIII I proposed a new mixed dynamic SGS model. The reader will find that they are written in an evolutionary way. As they represent my research over a period of four and a half years, the results presented in some papers are improvements on those reported in previous papers and the conclusions sometimes contradict those made earlier. The most important change in the conclusions is in the simulations of the flow around a bus. Good agreement in the velocity profiles between LES results and the experimental data was found in Paper V. Later, however (in Papers VI, IX and X), it was concluded that the experimental data are inaccurate. This evolution of knowledge resulted in Papers VII, VIII and X, which represent *the state of the art* for simulations of the flow around a cube, the mixed dynamic model and simulations of the flow around a bus, respectively.

6.1 Paper I

6.1.1 Motivation and background

Previous large-eddy simulations of the flow around a cube placed in a channel flow [56, 59] have proven to be superior to the RANS simulations [25] and to provide accurate results. These simulations used a

very fine computational grid and the inlet boundary condition obtained from a previous simulations of the channel flow with periodic boundary conditions. An extension of a simulation of this kind to higher Reynolds number characterizing the flow around a car would imply very high computational costs. My interest in this flow was not only to accurately predict the flow but to find a way to reduce the computational cost in simulations described in [56] and [59].

6.1.2 Work and results

The experimental profile (constant in time) was used at the inlet. This inlet condition contains no information on the turbulence. However, the strong separations at the front face edges minimize the influence of the upstream flow to the flow downstream of the front face. The computational grid was approximately four times coarser than the grids used in [56] and [59]. Two one-equation subgrid-scale (SGS) models were used to model the SGS stress tensor. The simulations that used these models were compared with a simulation made without a model.

Both simulations using one-equation models resulted in predicted flows in good agreement with experiments. The models gave similar results that were better than those of the simulation without a model. Both models have been shown to be able to predict the transport of SGS turbulent energy from small to large scales (backscatter). Although grid independence was not proven in this paper, it was shown that using a simple inlet condition, a relatively coarse grid and a one-equation model gives accurate results.

6.2 Paper II

6.2.1 Motivation and background

As shown in Paper I, the one-equation SGS models can predict a negative SGS dissipation of the resolved kinetic energy (the production term in the equation for SGS kinetic energy), indicating “backscatter”. This paper aimed to provide an explanation of this “backscatter” phenomenon.

6.2.2 Work and results

Two simulations were made, one of the flow in a plane channel and the other of the flow around the cube discussed in Paper I. Similar to the simulation of the flow around a cube, the channel flow simulations provided results that were in good agreement with previous LES and predicted "backscatter". The production terms for the resolved kinetic energy equation were studied with the aim of improving RANS models. Negative SGS dissipation of the resolved kinetic energy in the flow around a cube was found to occur near the front vertical corners of the cube. To explain this, the terms in the expression for the SGS dissipation of the resolved kinetic energy were studied, and it was found that the dynamic Leonard stress, L_{13}, was the dominant negative term.

6.3 Paper III

6.3.1 Motivation and background

Being a time-dependent three dimensional numerical technique, large-eddy simulation provides much more data than RANS or experimental studies. The extraction of the information from LES results is far from trivial and several different visualization techniques were suggested for representation of the flow features.

6.3.2 Work and results

This paper aimed to illustrate different techniques for the visualization in the test case of the flow around a cube. Besides the well established visualization techniques such as streamlines, velocity vector planes and the isosurface of the pressure, a relatively new technique with the second invariant of the velocity gradient was used. All these techniques proved to be useful and it was found that a combination of several techniques is needed for accurate representation of both instantaneous and time-averaged flows. For example, the isosurface of the time-averaged pressure was found to be best for visualization of the arch vortex behind the cube, whereas the isosurface of the instantaneous second invariant of the velocity gradient showed its superiority in representing the instantaneous coherent structures. Finally it was shown that the LES data obtained in the entire computational domain and for each time step can be used for simulations of real-life experiments.

6.3.3 Comments

In later papers (Papers V-VII, IX and X), we also used other visualization techniques such as the critical-point theory [11, 64].

6.4 Paper IV

6.4.1 Motivation and background

Besides the development of the LES technique for vehicle aerodynamics, this project aimed to improve our knowledge of the flow around these bodies. Thus the results of LES of the flow around a cube were used to study this flow and for comparison with the experimental observations and previous knowledge of similar flows.

6.4.2 Work and results

This paper presented both the instantaneous and the time-averaged flow around a cube. The time-averaged flow was found to consist of the horseshoe vortex, the secondary corner vortex upstream of the cube, lateral vortices, the vortex on the top of the cube, the secondary vortex behind the cube and the arch vortex in the separation bubble behind the cube. All these flow structures were found to be in good agreement with the experimental results. The main difference between the LES and the experimental results was in the position of the horseshoe legs. The explanation for this discrepancy was presented in the paper and was based on previous experimental observations.

6.5 Paper V

6.5.1 Motivation and background

Although LES of the flow around the cube has proven to provide accurate results, that flow is very different from the flow around a car. Thus a second test case that included more of the physics of the flow around a car was needed.

6.5.2 Work and results

The flow chosen was that around a simplified bus for which some experimental data exist [17, 18] and that was similar to the flow around Ahmed's body [2] which was used in a number of experimental studies. A Reynolds number of 0.21×10^6 based on the vehicle's high and the inlet velocity was considered to be high enough to produce a flow similar to that at higher Reynolds number of the flow around a real car. Relatively accurate results were obtained using a coarse grid and the approximate wall boundary conditions based on the instantaneous logarithmic low.

6.5.3 Comments

Good agreement was found in Paper V between the velocity profiles in LES results and in the experimental data. Later (in Papers VI, IX and X), however, it was concluded that the experimental data were inaccurate.

6.6 Paper VI

6.6.1 Motivation and background

While in channel flow the near-wall coherent structures must be resolved for the correct representation of the flow, the near-wall resolution can probably be relaxed for flow around bluff bodies such as cars, which is dominated by large flow structures. How fine a mesh is needed in such a flow is unknown, and grid refinement studies are needed to find optimal resolution.

6.6.2 Work and results

The computational grid used in Paper V was refined in Paper VI in the wall-normal direction only, and no-slip condition was applied on the solid walls. The resulting velocities in the wake region were in equally good or poorer agreement with the experiments as those in Paper V. The results for the pressure coefficient at the rear face of the bus and the length of the separation bubble behind the bus were only slightly improved. The most evident improvement in the new simulation was in the prediction of the thin vortices near the edges of the rear face of

the bus that were observed neither in the simulation in Paper V nor in the experiments.

6.7 Paper VII

6.7.1 Motivation and background

The surface streamlines downstream of the cube were found to be unsymmetrical in Papers I-IV, indicating that the averaging time in the simulations was too short. The simulations presented in these papers were made on only one computational grid, and no comparison with the previous LES was presented. Thus a longer averaging time was needed to obtain time-independent statistical averages, and a grid refinement study was needed to prove the grid independence of the results.

6.7.2 Work and results

The averaging time in the simulations in this paper was doubled as compared with the simulations in Papers I-IV. The number of averaging samples in this new simulation was found to be sufficient. To establish the grid independence of the results, computations were made on three computational grids. The results of these simulations were compared with those of previous LES [56, 59] and unsteady RANS [30] and it was found that our simulations on a much coarser computational grid provided results similar to those of the previous LES and better than those of the unsteady RANS simulations.

6.8 Paper VIII

6.8.1 Motivation and background

In a coarse LES, such as those in Papers I-IV, a substantial fraction of the turbulent energy is in the SGS motion, indicating the need for constructing a more accurate model. This can be achieved by incorporating a history effect through the transport equation for the SGS kinetic energy. Although such a model was proposed by Ghosal *et al.* [23], it was computationally expensive. Thus a computationally less expensive model was needed.

6.8.2 Work and results

This paper presented a mixed dynamic one-equation model that is computationally less expensive than the model by Ghosal *et al.* [23]. The scale-similarity part of the model is used for the description of the local energy transport, i.e. the energy transport between scales very close to the cut-off. The eddy viscosity part of the model is used to represent the non-local transfer of energy, i.e. the transfer between all scales smaller and larger than grid filter size. Properties of the model were investigated and it was found that it is Galilean invariant and realizable. Moreover, the approximately correct near-wall behavior of the model has been proven. The model was tested for both channel flow and the case of a surface-mounted cube [41]. It was found that the model gives accurate results in both cases.

6.8.3 Comments

This model was implemented in single block computational code [13] only. Its implementation in a multiblock code is more complex and the simulations using this model need more communication between blocks as compared to simulations using the Smagorinsky model [60].

6.9 Paper IX

6.9.1 Motivation and background

Two different near-wall resolutions were used in the simulations of the flow around a bus in Papers V and VI. None of these resolutions was sufficient to resolve the turbulence producing near-wall structures. Besides, it was found that the predicted velocities in Paper VI were in poorer agreement with experimental data than the results reported in Paper V, although this simulation used better spatial resolution than that in Paper V. Thus a new simulation that resolved more of the turbulent energy in the near-wall region was needed to identify the influence of the near-wall resolution on the results and to determine whether the good agreement of the LES results with the experimental data in Paper V was a result of the wall functions used for modeling the solid wall boundary condition or the poor accuracy of the experimental data. Finally, I wanted to construct a database for validation of RANS and hybrid RANS-LES simulations.

6.9.2 Work and results

A new LES using much finer resolution than those described in Papers V and VI was made. The results for the velocities in the separation bubble were in poorer agreement with the experimental data than those in Papers V and VI. Very high turbulent intensities were found in this region, which indicated that the hot-wire results were unreliable. Thus my suspicion that the experimental data for the velocities were not accurate was confirmed. The length of the separation bubble behind the bus was found to converge towards the experimental value with mesh refinement. Drag and lift results were compared with the experimental data from the experiment of a similar flow, and good agreement was found. The integrated value of the pressure coefficient was found to differ by 5% from that measured in the experiment. This was explained by the boundary layers that exist in the experiment on the side walls of the wind tunnel, which were not resolved in the simulations but were replaced with slip conditions.

6.9.3 Comments

Although the spatial resolution was very fine in this simulation, an additional grid refinement in the span-wise direction is needed to resolve all the near-wall structures. The present simulation was computationally expensive (the computation time with 40 SGI R10000 CPUs was $\simeq 2300$ hours (elapsed time) and computational resources for an additional simulation on a larger grid were not available. One way of obtaining the same blockage region in the experiment and the simulation that would result in the same pressure coefficient on the rear face of the bus would be to estimate the displacement thickness, δ^*, along the side walls of the channel and then to move the channel walls in the simulation towards the wind tunnel's plane of symmetry by δ^*.

6.10 Paper X

6.10.1 Motivation and background

Papers VI and IX presented some new flow features, such as thin longitudinal and transversal vortices close to edges of the bus, that were not observed in experiments and previous RANS simulations of the flow around similar bodies. Thus an explanation for these and other flow

structures was needed. I also wanted to summarize the results of all three simulations in one paper.

6.10.2 Work and results

This paper summarized the results of the three simulations presented in Papers V, VI and IX. Both the instantaneous and the time-averaged flows were explored and the mechanisms of formation of flow structures were explained. A great difference was found between the instantaneous and the time-averaged flows, in agreement with experimental observations.

6.10.3 Comments

The resolution of the low frequency change in the pressure on the rear face of the bus requires very long time averaging. Although I ran a simulation for over 3.2 months on 40 CPUs, the reliability of the small frequency of the rear-face pressure signal ($St = 0.061$) is weak. This, together with the costly grid refinement studies needed to prove the numerical accuracy, are the chief problems that must be overcome in large-eddy simulations of this kind of flow.

Bibliography

[1] S. R. Ahmed. Wake structures of typical automobile shapes. *ASME: Journal of Fluids Engineering*, 103:162–169, 1981.

[2] S. R. Ahmed, G. Ramm, and G. Faltin. Some salient features of the time averaged ground vehicle wake. SAE Paper 840300, 1984.

[3] K. Aoki, T. Ohbayashi, M. Zhu, and H. Miyata. Finite-volume simulation of 3-d vortical flow-fields about road vehicles with various after-body configuration. SAE Paper 931896, 1993.

[4] E. Balaras, C. Benocci, and U. Piomelli. Two-layer approximate boundary conditions for large-eddy simulations. *AIAA Journal*, 34(6):1111–1119, 1996.

[5] J. Barlow, R. Guterres, R. Ranzenbach, and J. Williams. Wake structures of rectangular bodies with radiused edges near a plane surface. SAE Paper 1999-01-0648, 1999.

[6] J. B. Barlow, R. Guterres, and R. Ranzenbach. Rectangular bodies with radiused edges in ground effect. AIAA paper 99-3153, 1999.

[7] P. W. Bearman. Near wake flows behind two- and three-dimensional bluff bodies. *Journal of Wind Engineering and Industrial Aerodynamics*, 69-71:33–54, 1997.

[8] P. W. Bearman, D. De Beer, E. Hamidy, and J. K. Harvey. The effect of a moving floor on wind-tunnel simulation of road vehicles. SAE Paper No. 880245, 1989.

[9] P. W. Bearman, J. P. Davis, and J. K. Harvey. Measurement of the structure of road vehicle wakes. *International Journal of Vehicle Design,Technological Advances in Vehicle Design Series, SP3, Impact of Aerodynamics on Vehicle Design*, pages 493–499, 1983.

[10] W. Cabot. Near-wall models in large eddy simulations of flow behind a backward-facing step. In *Annual Research Briefs 1996*, pages 199–210, Center for Turbulent Research, Stanford Univ./NASA Ames Reseach Center, 1996.

[11] M. S. Chong, A. E. Perry, and B. J. Cantwell. A general classification of three-dimensional flow fields. *Physics of Fluids*, 5(2):765–777, 1990.

[12] L. Davidson. Large eddy simulation: A dynamic one-equation subgrid model for three-dimensional recirculating flow. In *11th Int. Symp. on Turbulent Shear Flow*, volume 3, pages 26.1–26.6, Grenoble, 1997.

[13] L. Davidson. Hybrid LES-RANS: A combination of a one-equation SGS model and a $k-\omega$ model for predicting recirculating flows. In *ECCOMAS CFD Conference*, Swansea, U.K., 2001.

[14] L. Davidson and B. Farhanieh. CALC-BFC: A finite-volume code employing collocated variable arrangement and cartesian velocity components for computation of fluid flow and heat transfer in complex three-dimensional geometries. Report 95/11, Dept. of Thermo and Fluid Dynamics, Chalmers University of Technology, Gothenburg, 1995.

[15] L. Davidson and S.-H. Peng. A hybrid LES–RANS model based on a one-equation SGS model and a two-equation $k-\omega$ model. In E. Lindborg, A. Johansson, J. Eaton, J. Humphrey, N. Kasagi, M. Leschziner, and M. Sommerfeld, editors, *The Second International Symp. on Turbulence and Shear Flow Phenomena*, volume 2, pages 175–180, Stockholm, 2001.

[16] J.W. Deardorff. A numerical study of the three-dimensional turbulent channel flow at large Reynolds numbers. *Journal of Fluid Mechanics*, 41:453–480, 1970.

[17] E. G. Duell. *Experimental investigation of unsteady near wakes of ground vehicle bodies*. PhD thesis, Cornell University, 1994.

[18] E. G. Duell and A. R. George. Experimental study of a ground vehicle body unsteady near wake. SAE Paper 1999-01-0812, 1999.

[19] P. Emvin. *The full multigrid method applied to turbulent flow in ventilated enclosures using structured and unstructured grids*.

PhD thesis, Department of Thermo and Fluid Dynamics, Chalmers University of Technology, Gothenburg, 1997.

[20] J. B. Freund. Noise sources in a low-Reynolds-number turbulent jet at Mach 0.9. *J. Fluid Mech.*, 438:277–305, 2001.

[21] R. Friedrich and M. Arnal. Analysing turbulent backward-facing step flow with a lowpass-filtered Navier-Stokes equations. *J. Wind. Engng. Ind. Aerodyn.*, 35:101–128, 1990.

[22] M. Germano, U. Piomelli, P. Moin, and W.H. Cabot. A dynamic subgrid-scale eddy viscosity model. *Physics of Fluids*, 3(7):1760–1765, 1991.

[23] S. Ghosal, T.S. Lund, P. Moin, and K. Akselvoll. A dynamic localization model for large-eddy simulation of turbulent flows. *Journal of Fluid Mechanics*, 286:229–255, March 1995.

[24] T. Han. Computational analysis of three-dimensional turbulent flow around a bluff body in ground proximity. *AIAA Journal*, 27(9):1213–1219, 1989.

[25] K. Hanjalić and S. Obi. ERCOFTAC/IAHR/COST workshop on refined flow modeling. pages 131–225, Delft University of Technology, 1997.

[26] M. Hashiguchi, K. Kawaguchi, R. Yamasake, and K. Kuwahara. Computational study of the wake structure of a simplified ground-vehicle shape with base slant. SAE Paper 890597, 1989.

[27] W-H. Hucho. *Aerodynamics of Road Vehicles*. Society of Automotive Engineers, Inc., 4 edition, 1998. ISBN 0-7680-0029-7.

[28] J. C. R. Hunt, C. J. Abell, J. A. Peterka, and H. Woo. Kinematical studies of the flows around free or surface-mounted obstacles; applying topology to flow visualization. *Journal of Fluid Mechanics*, 86:179–200, 1978.

[29] H.J. Hussein and R. J. Martinuzzi. Energy balance for turbulent flow around a surface mounted cube placed in a channel. *Physics of Fluids*, 8(3):764–780, 1996.

[30] G. Iaccarino and P. Durbin. Unsteady 3D RANS simulations using the $v^2 - f$ model. In *Annual Research Briefs 2000*, pages 263–269, Stanford University, 2000.

[31] H.J. Kaltenbach, M. Fatica, R. Mittal, T.S. Lund, and P. Moin. Study of flow in plane asymmetric diffuser using large-eddy simulation. *Journal of Fluid Mechanics*, 390:151 – 186, 1999.

[32] T. Kataoka, H. China, K. Nakagawa, K. Yanagimoto, and M. Yoshida. Numerical simulation of road vehicle aerodynamics and effect of aerodynamic devices. SAE Paper 910597, 1991.

[33] S.J. Kline, W.C. Reynolds, F.A. Schraub, and P.W. Runstadler. The structure of turbulent boundary layers. *Journal of Fluid Mechanics*, 30:741–773, 1967.

[34] S. Krajnović and L. Davidson. Large eddy simulation of the flow around a bluff body. *AIAA Journal*, 40(5):927–936, 2002.

[35] S. Krajnović and L. Davidson. A mixed one-equation subgrid model for large-eddy simulation. *Int. J. Heat and Fluid Flow*, 23(4):413–425, 2002.

[36] S. Krajnović and L. Davidson. Numerical study of the flow around the bus-shaped body. 2002. submitted for journal publication.

[37] S. Krajnović and L. Davidson. A test case for large-eddy simulation in vehicle aerodynamics. In *Proceedings of the 5th International Symposium on Engineering Turbulence Modelling and Measurements*, Mallorca, Spain, 2002.

[38] A. Larousse, R. Martinuzzi, and C. Tropea. Flow around surface-mounted, three-dimensional obstacles. In *9th Int. Symp. on Turbulent Shear Flow*, pages 127–139, Munich, 1991. Springer-Verlag.

[39] D.K. Lilly. A proposed modification of the Germano subgrid-scale closure method. *Physics of Fluids*, 4(3):633–635, 1992.

[40] S. Liu, C. Meneveau, and J. Katz. On the properties of similarity subgrid-scale models as deduced from measurements in a turbulent jet. *Journal of Fluid Mechanics*, 275:83–119, 1994.

[41] R. Martinuzzi and C. Tropea. The flow around surface-mounted prismatic obstacles placed in a fully developed channel flow. *ASME: Journal of Fluids Engineering*, 115(1):85–91, 1993.

[42] C. Menevau, T. S. Lund, and W. H. Cabot. A lagrangian dynamic subgrid-scale model of turbulence. *Journal of Fluid Mechanics*, 319:353–385, 1996.

[43] C. Meneveau and J. Katz. Scale-invariance and turbulence models for large-eddy simulation. *Ann. Rev. Fluid Mech.*, 32:1–32, 2000.

[44] S. Menon and W.-W. Kim. High Reynolds number flow simulations using the localized dynamic subgrid-scale model. 34th Aerospace Sciences Meeting, AIAA Paper 96-0425, Reno, 1996.

[45] P. Moin and K. Mahesh. Direct numerical simulation: A tool in turbulence research. *Ann. Rev. Fluid Mech.*, 30:539–578, 1998.

[46] H. Nilsson. *Numerical Investigations of Turbulent Flow in Water Turbines*. PhD thesis, Department of Thermo and Fluid Dynamics, Chalmers University of Technology, Gothenburg, 2002. ISBN 91-7291-187-5.

[47] H. Nilsson and L. Davidson. CALC-PVM: A parallel SIMPLEC multiblock solver for turbulent flow in complex domains. Internal report 98/12, Department of Thermo and Fluid Dynamics, Chalmers University of Technology, Gothenburg, 1998.

[48] A. E. Perry and M. S. Chong. A description of eddying motions and flow patterns using critical-point concepts. *Ann. Rev. Fluid Mech.*, 19:125–155, 1987.

[49] U. Piomelli and J.R. Chasnov. Large-eddy simulations: Theory and applications. In D. Henningson, M. Hallbaeck, H. Alfreddson, and A. Johansson, editors, *Transition and Turbulence Modelling*, pages 269–336, Dordrecht, 1996. Kluwer Academic Publishers.

[50] U. Piomelli, J. Ferziger, and P. Moin. New approximate boundary conditions for large eddy simulations. *Physics of Fluids A*, 1:1061–1068, 1989.

[51] S. B. Pope. *Turbulent Flows*. Cambridge University Press, Cambridge, first edition, 2000.

[52] C.M. Rhie and W.L. Chow. Numerical study of the turbulent flow past an airfoil with trailing edge separation. *AIAA Journal*, 21(11):1525–1532, 1983.

[53] S. K. Robinson. Coherent motions in the turbulent boundary layer. *Ann. Rev. Fluid Mech.*, 23:601–639, 1991.

[54] W. Rodi. Large-eddy simulations of the flow past bluff bodies: State-of-the-art. In *Proc. JSME Centennial Grand Conf., Int. Conf. Fluid Eng.*, Tokyo, 1997.

[55] W. Rodi, J. H. Ferziger, M. Breuer, and M. Pourquié. Workshop on LES of flows past bluff bodies. Rotach-Egern, Germany, 1995.

[56] W. Rodi, J.H. Ferziger, M. Breuer, and M. Pourquié. Status of large-eddy simulations: Results of a workshop. *J. Fluids Engineering*, (2):248–262, 1997.

[57] H. Schlichting. *Boundary-Layer Theory*. McGraw-Hill, New York, seventh edition, 1979.

[58] U. Schumann. Subgrid scale model for finite difference simulations of turbulent flows in plane channels and annuli. *J. Comp. Phys.*, 18:376–404, 1975.

[59] K. B. Shah and J. H. Ferziger. A fluid mechanicians view of wind engineering: Large eddy simulation of flow past a cubic obstacle. *Journal of Wind Engineering and Industrial Aerodynamics*, 67:211–224, April 1997.

[60] J. Smagorinsky. General circulation experiments with the primitive equations. *Monthly Weather Review*, 91(3):99–165, 1963.

[61] C. R. Smith and S. P. Metzler. The characteristics of low-speed streaks in the near-wall region of a turbulent boundary layer. *Journal of Fluid Mechanics*, 129:27–54, 1983.

[62] P. R. Spalart, W. H. Jou, M. Strelets, and S. R. Allmaras. Detached-eddy simulation of an airfoil at high angle of attack. In *Advances in DNS/LES, Proceedings of the First AFOSR International Conference on DNS/LES*, 1997.

[63] A. Spohn and P. Gillieron. Flow separations generated by a simplified geometry of an automotive vehicle. In *IUTAM Symposium: Unsteady Separated Flows*, April 8-12, Toulouse, France, 2002.

[64] D. Sujudi and R. Haimes. Identification of swirling flow in 3-D vector fields. AIAA Paper AIAA 95-1715, 1995.

[65] Y. Zang, R.L. Street, and J.R. Koseff. Application of a dynamic subgrid-scale model to turbulent recirculating flows. Technical report, Center for Turbulence Research, Annual Research Briefs, 1992.

Paper I

Comparison of Two One-Equation Subgrid Models in Recirculating Flows

S. Krajnović, D. Müller and L. Davidson

In Proceedings of *Direct and Large-Eddy Simulation III*, Eds: P.V. Voke, N.D. Sandham and L. Kleiser, pages 63-74, 1999.

Paper II

Large-eddy simulation of the flow around a surface-mounted cube using a dynamic one-equation subgrid model

S. Krajnović and L. Davidson

In Proceedings of *The First International Symp. on Turbulence and Shear Flow Phenomena*, Santa Barbara, Eds: S. Banerjee & J.K. Eaton, begell house, inc., New York, Wallingford U.K., pages 741-746, 1999.

Paper III

Flow around a three-dimensional bluff body

S. Krajnović and L. Davidson

In Proceedings of the *9th International Symposium on Flow Visualisation*, Heriot-Watt University, Edinburgh, G.M. Carlomagno and I. Grant (Eds.), 2000.

Paper IV

Large-Eddy Simulation of the Flow Around a Three-Dimensional Bluff Body

S. Krajnović and L. Davidson

AIAA paper 2001–0432, Reno, NV, 2001.

Paper V

Large-Eddy Simulation of the Flow Around a Ground Vehicle Body

S. Krajnović and L. Davidson

SAE Paper 2001-01-0702, Detroit, 2001.

Paper VI

Large-Eddy Simulations of the Flow Around A Simplified Bus

S. Krajnović and L. Davidson

In Proceedings of the *3rd AFOSR International Conference on DNS and LES*, Eds: C. Liu and L. Sakell and T. Beutner, Arlington, Texas, pages 775-782, 2001.

Paper VII

Large-Eddy Simulation of the Flow Around a Bluff Body

S. Krajnović and L. Davidson

AIAA Journal, 40(5), pages 927-139, 2002.

Paper VIII

A mixed one-equation subgrid model for large-eddy simulation

S. Krajnović and L. Davidson

International Journal of Heat and Fluid Flow, 23(4), pages 413-245, 2002.

Paper IX

A test case for large-eddy simulation in vehicle aerodynamics

S. Krajnović and L. Davidson

In Proceedings of the *5th International Symposium on Engineering Turbulence Modelling and Measurements, Mallorca, Spain*, 2002.

Paper X

Numerical study of the flow around the bus-shaped body

S. Krajnović and L. Davidson

Submitted for journal publication.